

Quantum circuits measuring weak values and Kirkwood–Dirac quasiprobability distributions, with applications

Rafael Wagner,^{1, 2, *} Zohar Schwartzman-Nowik,^{3, 4} Ismael L. Paiva,^{4, 5} Amit Te’eni,⁴ Antonio Ruiz-Molero,^{1, 6} Rui Soares Barbosa,¹ Eliahu Cohen,⁴ and Ernesto F. Galvão^{1, 7, †}

¹*INL – International Iberian Nanotechnology Laboratory, Braga, Portugal*

²*Centro de Física, Universidade do Minho, Braga, Portugal*

³*School of Computer Science and Engineering, Hebrew University, Jerusalem, Israel*

⁴*Faculty of Engineering and the Institute of Nanotechnology and Advanced Materials, Bar Ilan University, Ramat Gan, Israel*

⁵*H. H. Wills Physics Laboratory, University of Bristol, Bristol, United Kingdom*

⁶*Departamento de Informática, Universidade do Minho, Braga, Portugal*

⁷*Instituto de Física, Universidade Federal Fluminense, Niterói – RJ, Brazil*

(Dated: February 3, 2023)

Weak values and Kirkwood–Dirac (KD) quasiprobability distributions have been independently associated with both foundational issues in quantum theory and advantages in quantum metrology. We propose simple quantum circuits to measure weak values, KD distributions, and density matrix spectra without the need for post-selection. This is achieved by measuring unitary-invariant, relational properties of quantum states, as functions of Bargmann invariants. Our circuits also enable direct experimental implementation of various applications of KD distributions, such as out-of-time-ordered correlators (OTOCs) and the quantum Fisher information in post-selected parameter estimation, among others. This results in a unified view of nonclassicality in all those tasks. In particular, we discuss how negativity and imaginarity of Bargmann invariants relate to set coherence.

CONTENTS

I. Introduction	1	A. Formal comparison between standard weak measurement and circuit protocol	15
II. Preliminaries	2	1. Same number of samples for numerator and denominator	16
A. Weak values	2	2. Different number of samples for numerator and denominator	17
B. Kirkwood–Dirac quasiprobability distribution	3	B. Sample and measurement complexity of estimating the spectrum using the cycle-test	18
III. Quantum circuits for measuring weak values and Kirkwood–Dirac quasiprobability distributions	4	1. Proof of Lemma 2	18
A. Bargmann invariants	4	2. Numerical analysis for the Faddeev–LeVerrier algorithm	19
B. Applications of third order invariants	5	a. Learning the largest eigenvalue	20
1. Kirkwood–Dirac quasiprobability	5	C. Proof of Lemma 6	20
2. Weak values	5		
C. Applications for circuits measuring higher-order invariants	7		
1. Post-selected quantum Fisher information	7	I. INTRODUCTION	
2. Out-of-time-ordered correlators	7		
3. Estimating the spectrum	8		
IV. Minimal experimental conditions for witnessing nonclassicality	10	Two quantities have profoundly impacted quantum foundations, metrology, and thermodynamics: weak values, introduced in the seminal work of Aharonov, Albert, and Vaidman [1], and the quasiprobability distribution introduced by Kirkwood and Dirac [2, 3]. These were recently connected with one another [4], and both can be experimentally measured using weak measurement schemes involving pre- and post-selection of carefully chosen observables [5]. Despite such great impact, investigations of measurement schemes that can be implemented using currently relevant quantum circuit architectures without post-selection and without weak coupling are only now beginning to appear [5, 6].	
V. Discussion and future directions	12		
Acknowledgments	13	Here, we propose a unified framework that enables expressing both Kirkwood–Dirac (KD) quasiprobability	
References	13		

* rafael.wagner@inl.int

† ernesto.galvao@inl.int

functions and weak values in terms of more fundamental quantities, known as Bargmann invariants. These invariants characterize the relational properties of a set of quantum states, that is, all the properties that remain invariant under the application of a unitary to all states in the set. The simplest Bargmann invariant is the overlap $\text{Tr}(\rho\sigma)$ between two states ρ and σ , which is also the easiest to probe experimentally [7].

KD distributions and weak values exhibit nonclassicality, in the sense of assuming negative or even complex values outside of the classically allowed range. As it turns out, the nonclassicality of KD distributions and weak values, which underpins their relevance as quantum information resources, is a relational property described by Bargmann invariants. We show that, in general, learning the values of higher-order invariants (beyond overlaps) is *necessary* to assess nonclassicality. We also show how further assumptions can be used to ascertain nonclassicality using only overlaps. Moreover, we point out some connections between nonclassicality and the notion of set coherence.

More pragmatically, the nonclassicality of weak values and KD distributions has been linked to quantum advantage in metrology [8] and to quantification of quantum information scrambling [9, 10]. Our framework describing those quantities via Bargmann invariants allows us to use recently proposed cycle test circuits [11, 12] to directly measure weak values and KD distributions. This enables direct quantum circuit measurements of quantities associated with multiple applications; see Fig. 1 for a conceptual scheme describing our main contributions. We compare the performance of these circuits with the usual strategies for performing weak measurements and quantum state tomography. We also show how out-of-time-ordered correlators (OTOCs), used to quantify information scrambling in quantum dynamics, can be directly measured using the same type of circuit. We show that this is also true of quantum Fisher information obtained in post-selected parameter estimation. As a final practical application, we describe circuits to estimate the spectrum of a given d -dimensional quantum state ρ via direct estimation of $\text{Tr}(\rho^n)$ for $n = 1, \dots, d$. We expect our contributions to open the path to the quantification of nonclassicality and many other applications; for example, in the characterization of coherence, entanglement, and quantum computational advantage.

This paper is organized as follows. In Sec. II, we introduce the basic definitions of KD distributions, weak values arising from weak measurements, and related quantities. In Sec. III, we present our main results, describing how one can experimentally access both quantities via the measurement of Bargmann invariants. We compare the efficiency and experimental particularities of estimating weak values using the standard weak measurement approach against quantum circuits. We also study how the measurement of higher-order Bargmann invariants enables the estimation of the quantum Fisher information obtained in post-selected parameter amplification, OTOCs, and the spectrum of a density matrix. In Sec. IV, we analyze minimal conditions for characterizing the nonclassicality of KD distributions and related quantities. We conclude in Sec. V with an outlook on possible future work.

II. PRELIMINARIES

A. Weak values

Consider a system prepared (pre-selected) in state $|\psi\rangle$, on which one performs a weak measurement of an observable A , i.e., a measurement associated with a small coupling strength (when compared to the standard deviation of the measuring pointer). Although this measurement has the apparent downside of not generating a significant average shift of the pointer compared to its standard deviation, it has the benefit of causing little disturbance to the system of interest. Finally, let the system be post-selected in the state $|\phi\rangle$. It turns out that for this post-selection the average shift of the pointer used for the intermediate weak measurement is proportional to

$$A_w := \frac{\langle \phi | A | \psi \rangle}{\langle \phi | \psi \rangle}, \quad (1)$$

which is known as the weak value of A [1]. This quantity may lie outside the spectrum of the measured operator, in which case the weak value is said to be *anomalous*. In fact, with appropriate choices of pre- and post-selections, anomalous weak values can be arbitrarily large and also have a non-vanishing imaginary part.

Due to the appearance of such anomalous values and to the usual way in which these quantities are experimentally obtained, via weak measurements, the quantum nature of weak values has been questioned since their introduction; see Ref. [13] for an overview. More recently, this situation seems to have changed, with the nonclassicality of certain weak values being more well established. Important theoretical results contributing to this understanding state that anomalous weak values from weak measurements constitute proofs of generalized contextuality [14, 15].

Since weak measurements cause little disturbance to the measured system, they also do not extract much information about it. As a result, protocols involving weak measurements typically require large ensembles in order to decrease the variance associated with them; see, however, the recent demonstration in Ref. [16]. In spite of this, weak values have found various practical applications. In particular, through a method known as *weak value amplification*, large weak values are used for realizing extremely sensitive measurements [17–29]. This technique is especially helpful in the presence of technical noise or detector saturation [21, 24].

Considering the spectral decomposition of the observable A , $A = \sum_{a \in \sigma(A)} a |a\rangle\langle a|$, with $\sigma(A)$ denoting the

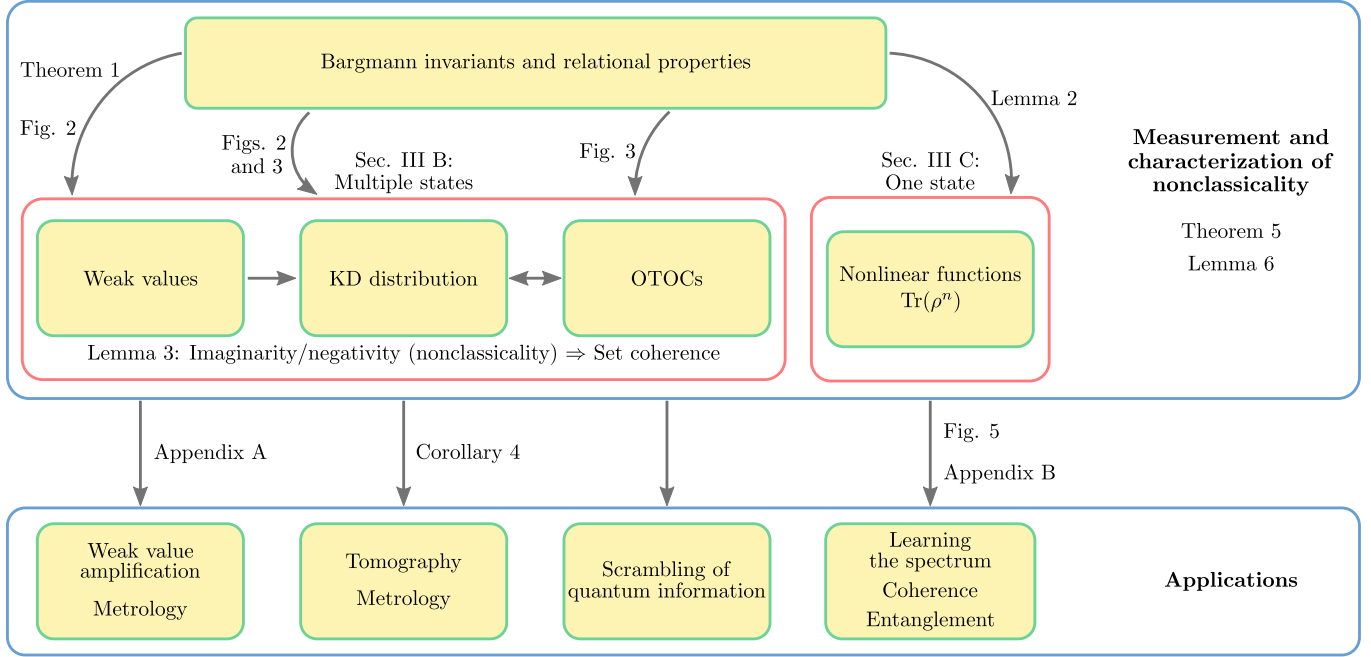


Figure 1. Conceptual scheme describing the content and main contributions and their inter-relations. We show how weak values, the Kirkwood–Dirac (KD) quasiprobability distribution, and out-of-time-ordered correlators (OTOCs) can all be expressed as unitary-invariant quantities known as Bargmann invariants. Circuits to measure those enable more direct implementations in many applications, as discussed in Sec. III. Moreover, results on the nonclassicality of Bargmann invariants, such as those obtained in Sec. IV, enable a better understanding and quantification of quantum advantage, where we show that negativity and imaginarity of Bargmann invariants require set coherence.

spectrum of A , we see that

$$A_w = \sum_{a \in \sigma(A)} a \frac{\langle \phi | a \rangle \langle a | \psi \rangle}{\langle \phi | \psi \rangle} = \sum_{a \in \sigma(A)} a \frac{\langle \phi | a \rangle \langle a | \psi \rangle \langle \psi | \phi \rangle}{|\langle \phi | \psi \rangle|^2} \quad (2)$$

since, by construction, $\langle \phi | \psi \rangle \neq 0$. It so happens that the numerators in the expression for the weak value above correspond to values of the KD quasiprobability distribution at the phase-space point determined by the pre- and post-selected states. These have their own relevance in quantum information theory [4]. We now proceed to review some basic facts on the KD quasiprobability distribution.

B. Kirkwood–Dirac quasiprobability distribution

Consider a finite discrete phase space $I \times F$ associated with quantum states $\{|i\rangle\}_{i \in I}$ and $\{|f\rangle\}_{f \in F}$ that form two orthonormal bases of a d -dimensional Hilbert space \mathcal{H} . The KD quasiprobability distribution for a given state $\rho \in \mathcal{D}(\mathcal{H})$ ¹ is given by

$$\xi(\rho | i, f) := \langle f | i \rangle \langle i | \rho | f \rangle. \quad (3)$$

Under the assumption that $\langle f | i \rangle \neq 0$ for all i, f , the KD distribution provides complete information on the state ρ . This is because, in this case, the values of the KD distribution at phase-space points are the decomposition coefficients with respect to the orthonormal basis $\{|i\rangle \langle f| / \langle f | i \rangle\}_{(i,f) \in I \times F}$ of $\mathcal{B}(\mathcal{H})$, the space of bounded operators on \mathcal{H} .

The KD distribution can be *extended* to be well defined for a larger number of bases, or even general projection-valued measures (PVMs). For a family of PVMs $M_i = \{\Pi_k^i\}_k$, with $i = 1, \dots, n$, the extended KD distribution reads

$$\xi(\rho | k_1, \dots, k_n) = \text{Tr}(\Pi_{k_1}^1 \Pi_{k_2}^2 \dots \Pi_{k_n}^n \rho). \quad (4)$$

The KD distribution and its extended variants are key quantities witnessing many nonclassical properties of quantum dynamics [4, 5]. Let us focus on a recently found connection with quantum metrology [8]. For benchmarking proof-of-principle experiments in metrology, it is important that the quantum Fisher information in the linear regime and the post-selected quantum Fisher information can both be described in terms of KD distributions [5]. The quantum Fisher information provides the optimal rate with which one can learn some (set of) parameter(s) θ encoded in quantum states ρ_θ via the Cramér–Rao bound [30, 31]. For good introductory works on Fisher information theory and quantum or classical estimation theory, see, e.g., Refs. [32–34]. It

¹ We denote by $\mathcal{D}(\mathcal{H})$ the set of all quantum states in the Hilbert space \mathcal{H} .

is therefore interesting from a foundational perspective to seek ways of estimating the quantum Fisher information, an important task for the noisy intermediate-scale quantum (NISQ) era of technological capabilities [35–37]. Indeed, this is currently an active research topic [38, 39].

Ref. [8] connected nonclassicality of the KD distribution with metrological advantage in parameter estimation. The following relation was established between the extended KD distribution and the quantum Fisher information of post-selected states:

$$\mathcal{I}^{\text{ps}} = 4 \sum_{i, i', f} \lambda_i \lambda_{i'} \frac{\xi(\rho_\theta | i, i', f)}{p_\theta^{\text{ps}}} - 4 \left| \sum_{i, i', f} \lambda_i \frac{\xi(\rho_\theta | i, i', f)}{p_\theta^{\text{ps}}} \right|^2. \quad (5)$$

Here, \mathcal{I}^{ps} stands for the quantum Fisher information calculated for a state ρ that, after having encoded information about a parameter θ through an evolution to state ρ_θ by some $U = e^{-i\theta I}$ with the Hamiltonian $I = \sum_i \lambda_i |i\rangle\langle i|$ a known observable, it is successfully post-selected with respect to some projector $F = \sum_f |f\rangle\langle f|$ with success probability $p_\theta^{\text{ps}} = \text{Tr}(F\rho_\theta)$. The extended KD distribution for this scenario takes the form

$$\xi(\rho_\theta | i, i', f) = \langle i | \rho_\theta | i' \rangle \langle i' | f \rangle \langle f | i \rangle. \quad (6)$$

This relation allowed to experimentally address the metrological advantages of post-selected parameter amplification for the estimation of a small parameter θ in Ref. [40]. In Ref. [41], the authors bounded the efficiency of the advantage, formally relating the growth of the post-selected version of Fisher information with the factor p_θ^{ps} . As a remark, the KD distribution also appears as part of the quantum Fisher information without the need for post-processing in the so-called linear response regime, as discussed in Ref. [5].

In Ref. [4] it was shown that the extended KD distribution underlies the out-of-time-ordered correlators (OTOCs) that are commonly used to witness the scrambling of quantum information. These quantities are given by

$$\text{OTOC}(t) := \text{Tr}(W^\dagger(t) V^\dagger W(t) V \rho). \quad (7)$$

Intuitively, OTOCs witness scrambling of information in the following situation. Consider a many-body system ρ and two observables W and V acting over non-local regions of the system (the canonical example being observables acting on the initial and final spins in a one-dimensional lattice of size $N \gg 1$). The function $\text{OTOC}(t)$ witnesses the non-commutativity of the observable $W(t) = U(t)^\dagger \Pi_w^W U(t)$, in the Heisenberg picture of unitary evolution by $U(t)$, with respect to V . It thus signals the delocalization of quantum information. The OTOC can be written as [4]

$$\sum_{v_1, w_2, v_2, w_3} v_1 w_2 v_2^* w_3^* \text{Tr}(\Pi_{w_3}^{W(t)} \Pi_{v_2}^V \Pi_{w_2}^{W(t)} \Pi_{v_1}^V \rho), \quad (8)$$

where v and w are eigenvalues of V and $W(t)$, respectively, associated with projectors Π_v^V and $\Pi_w^{W(t)}$. We also have that $\Pi_w^{W(t)} = U(t)^\dagger \Pi_w^W U(t)$. The choice of labels made in Eq. (8) arises from the interpretation of Ref. [4] for which the OTOC is described by a quasiprobability naturally arising from comparing forward and backward evolution of the system under the action of a unitary operator U .

The coarse-graining hides the possible degeneracy in the spectral decomposition of the observables. In fact, if we take such degeneracy into account, we have that each observable is described by

$$\Pi_v^V = \sum_{\lambda_v} |v, \lambda_v\rangle\langle v, \lambda_v|, \quad (9)$$

where the eigenspace associated with eigenvalue v is described by the complete set of vectors $|v, \lambda_v\rangle$ with λ_v ranging over the degeneracy parameters. We find that the OTOC can be described in a more fine-grained way by

$$\text{OTOC}(t) = \sum_{(v_1, \lambda_{v_1}), (v_2, \lambda_{v_2}), (w_2, \lambda_{w_2}), (w_3, \lambda_{w_3})} v_1 w_2 v_2^* w_3^* \tilde{A}_\rho, \quad (10)$$

where $\tilde{A}_\rho = \tilde{A}_\rho(v_1, \lambda_{v_1}; w_2, \lambda_{w_2}; v_2, \lambda_{v_2}; w_3, \lambda_{w_3})$ is the quasiprobability behind the OTOC [4]. This is an extended KD distribution given at each phase-space point by

$$\tilde{A}_\rho = \langle w_3, \lambda_{w_3} | U | v_2, \lambda_{v_2} \rangle \langle v_2, \lambda_{v_2} | U^\dagger | w_2, \lambda_{w_2} \rangle \times \langle w_2, \lambda_{w_2} | U | v_1, \lambda_{v_1} \rangle \langle v_1, \lambda_{v_1} | \rho U^\dagger | w_3, \lambda_{w_3} \rangle, \quad (11)$$

where each state $|v_l, \lambda_{v_l}\rangle\langle v_l, \lambda_{v_l}|$ corresponds to the state of the system after a measurement (related to observable V) was performed over it and an outcome (v_l, λ_{v_l}) was obtained, and similarly for W .

As we will shortly see, the various fundamental concepts discussed so far—more precisely, the KD distribution (Eq. (3)), its extended versions (Eq. (4)), the quasiprobability behind the OTOC (Eq. (11)), and the expression for weak values (Eq. (2))—are written in terms of Bargmann invariants. We review these quantities in the next section.

III. QUANTUM CIRCUITS FOR MEASURING WEAK VALUES AND KIRKWOOD–DIRAC QUASIPROBABILITY DISTRIBUTIONS

A. Bargmann invariants

General multivariate traces of quantum states can be directly measured in an efficient manner using the cycle test scheme [11], or constant depth circuit variations thereof [12]. These are the so-called n -th order Bargmann invariants:

$$\Delta_n(\rho_1, \dots, \rho_n) = \text{Tr}(\rho_1 \dots \rho_n). \quad (12)$$

These quantities are invariant under the simultaneous conjugation $\rho_i \mapsto Z\rho_iZ^{-1}$ by any invertible matrix Z . Invariant theory has studied Bargmann invariants in depth since they completely generate the ring of invariants over matrix tuples [42]. In Ref. [11], it was pointed out that this feature can be precisely used to completely characterize the equivalence class of all unitarily equivalent tuples, i.e., tuples that are mapped to one another by a unitary map $\rho_i \mapsto U\rho_iU^\dagger$. This implies that one can find sufficient conditions to witness the non-existence of a reference basis that simultaneously diagonalizes all states in a given tuple $(\rho_i)_i$, a property recently formalized within the resource theoretical framework and termed set coherence [43]. As shown in Ref. [11], negativity or imaginarity of Bargmann invariants witnesses this form of basis-independent coherence for a set of states.

Therefore, Bargmann invariants represent the unifying link for directly measuring and addressing the nonclassicality of KD distributions and weak values since both can be written as a function of third-order invariants, as we will see. In Ref. [11], third-order invariants play an important role since, for specific experimental setups, they not only witness but completely characterize set coherence of a tuple of pure states. We now address the specifics of experimentally estimating and applying such ideas to weak values and KD distributions based on third-order invariants.

B. Applications of third order invariants

1. Kirkwood–Dirac quasiprobability

In Fig. 2(a), we present a circuit for measuring the invariants defining the KD quasiprobability associated with pure state $|\psi\rangle$ at each phase-space point, $\xi(\psi|i, f) = \langle f|i\rangle\langle i|\psi\rangle\langle\psi|f\rangle$. The circuit, known as a cycle test [11], can be straightforwardly generalized to measure any invariant $\text{Tr}(\Pi_{k_1}^1 \dots \Pi_{k_n}^n \rho)$ of extended KD distributions. While here we focus on the case of pure states, the same architecture is capable of characterizing d -dimensional mixed input states.

Assuming that we can prepare states $|\psi\rangle$, $|i\rangle$, and $|f\rangle$ for any $i \in I$ and $f \in F$, the circuit in Fig. 2(a) measures the (real and imaginary part of) third-order invariants defining phase-space point values of the KD distribution of $|\psi\rangle$, to precision ε , with high probability, using $O(1/\varepsilon^2)$ samples of the triplet of states [12], and therefore constant order of samples of the state $|\psi\rangle$. The above protocol can estimate the entire KD distribution for any dimension with a total of $\tilde{O}(d^2/\varepsilon^2)$ samples with high probability, where the tilde hides $\log(d)$ terms. Assuming that $\langle i|f\rangle \neq 0$, learning the full KD distribution associated with a state can be used to perform full tomography [44].

Tomography via KD distribution is neither better nor worse in terms of sample and measurement complexity than textbook quantum state tomography using Pauli

measurements, which requires $O(d^4/\varepsilon^2)$ samples [45, 46], with high probability relative to the trace distance. If we learn the value of the KD distribution of ρ for every possible outcome of I and F , i.e., at every phase-space point, we can completely reconstruct the state ρ by

$$\rho = \sum_{(i,f) \in I \times F} \frac{|i\rangle\langle f|}{\langle i|f\rangle} \xi(\rho|i, f) \quad (13)$$

(in fact, this holds for any observable [4]). We now count the number of samples and measurements needed to perform tomography in this fashion, where we use cycle tests to estimate each $\xi(\rho|i, f)$ as the measurements. In order to estimate the value at each phase-space point up to precision ε with probability $1 - \delta$, we need $O(\ln(2/\delta)/\varepsilon^2)$ samples, a bound provided by the Hoeffding concentration inequality [47, 48]. Assuming that we want to estimate at every phase-space point with the same precision ε with probability $1 - \delta$, the number of samples is of the order of $\tilde{O}(d^2/\varepsilon^2)$, where we also hide the factors δ , as it is common to assume it to be fixed.

To compare this scaling in samples with standard tomography, we want to quantify the success of the procedure in terms of the distance induced by the 1-norm. Assuming that the KD phase-space values are ε_1 -close to the ideal, we have

$$\begin{aligned} \|\rho - \hat{\rho}\|_1 &= \left\| \sum_{ij} \frac{|i\rangle\langle f|}{\langle i|f\rangle} (\xi(\rho|i, f) - \hat{\xi}(\rho|i, f)) \right\|_1 \\ &\leq \varepsilon_1 \left\| \sum_{ij} P_{ij} \right\|_1 = \varepsilon_1 \|\mathbb{1}_{d \times d}\|_1 = \varepsilon_1 d, \end{aligned} \quad (14)$$

where $\hat{\xi}$ is the estimated KD distribution from the cycle test and $P_{ij} \equiv |i\rangle\langle j|/\langle i|f\rangle$ are the projectors in the basis of $\mathcal{B}(\mathcal{H})$. We have used that, by assumption, we have $|\xi(\rho|i, f) - \hat{\xi}(\rho|i, f)| \leq \varepsilon_1$ for all i, f . Therefore, in total, one needs $\tilde{O}(d^4/\varepsilon^2)$ samples to perform full KD state tomography ε close in the trace distance.

However, from the above calculation, it is clear that full tomography is *not needed* for having arbitrarily good precision in learning the KD distribution of a given state ρ . Therefore, in scenarios for which we connect the extended KD distribution of states to important quantities, such as the quantum Fisher information or the OTOC, there is a polynomial advantage in the sample complexity with respect to performing Pauli-based full tomography or even efficient incoherent full tomography [49].

2. Weak values

Weak values are other interesting quantities that can be measured by estimating third-order invariants. From Eq. (2), we recognize that

$$\langle A \rangle_w = \sum_{a \in \sigma(A)} a \frac{\Delta_3(\phi, a, \psi)}{\Delta_2(\phi, \psi)}. \quad (15)$$

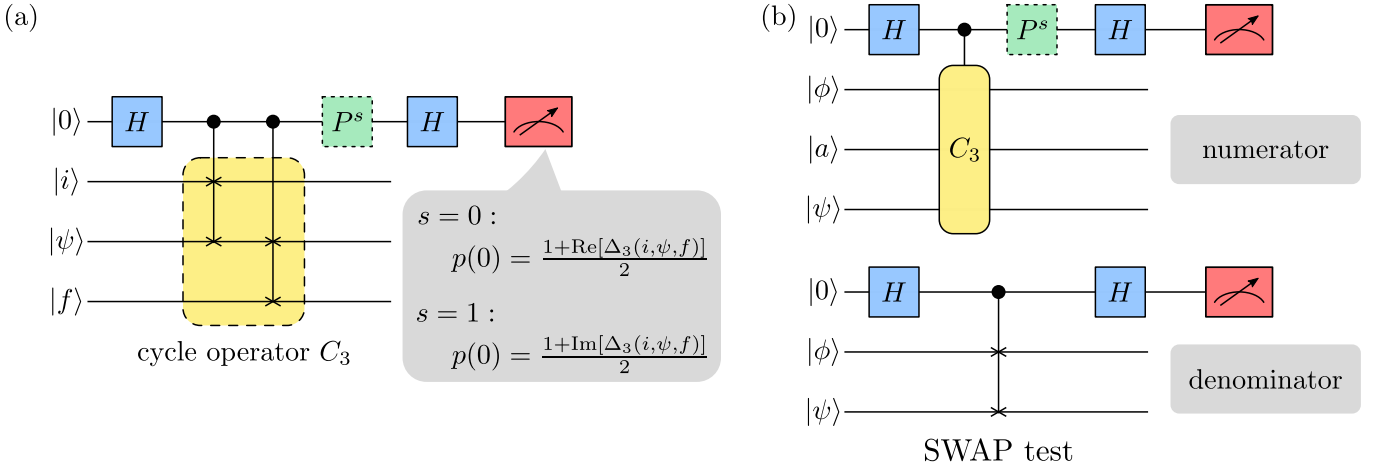


Figure 2. **Quantum circuits for measuring the third-order Bargmann invariants characterizing (a) Kirkwood-Dirac quasiprobability distribution and (b) weak values.** Circuit (a) assumes that one can prepare basis states from the two bases $\{|i\rangle\}_i, \{|f\rangle\}_f$ defining the KD distribution, as well as the state $|\psi\rangle$ to be characterized. Two variations of the circuit estimate the real and imaginary parts of the value of the KD distribution at a chosen phase-space point. For the circuit in (b), we require input states that are eigenvectors $\{|a\rangle\}_a$ of an observable A , as well as the pre- and post-selection states used in the standard weak measurement protocol. On top of that, anomalous weak values result from precisely selecting the overlaps $|\langle\phi|\psi\rangle|^2$, which can be directly measured using the two-state SWAP test.

Thus, assuming that we have means to prepare the eigenstates $\{|a\rangle\}_a$ of A , the same protocol can measure the weak value of A by estimating the relevant Bargmann invariants of orders 3 and 2.

This observation implies that weak values can be inferred without the need for post-selection, up to any desired accuracy, using the cycle test circuits to measure Bargmann invariants. In Fig. 2(b), we show the circuits for measuring weak values, which require the preparation of the states corresponding to the pre- and post-processing together with all eigenvectors of the observable A in parallel and the application of the controlled cycle operation with the help of a single auxiliary qubit.

The nonclassicality of weak values, witnessed by anomalous negative and imaginary values, can also be directly estimated using the above circuit and analyzed through the lens of Bargmann invariant nonclassicality. This result dissociates once more weak values from weak measurements, similarly to the discussions in Refs. [6, 50, 51]. Beyond that, it provides a new perspective on the physical and operational meaning of weak values as a *relational quantity* between pre- and post-selection states and the eigenstates of a given observable A . This connects the nonclassicality of weak values with quantum coherence, a topic that we revisit in Sec. IV.

The lack of post-selection might suggest that the sample complexity for measuring weak values using the cycle test improves over the standard weak measurement protocol. The following theorem shows that this is not the case. In fact, if the overlap between the pre- and post-selection is small, our bounds suggest that the cycle test performs worse.

Theorem 1. *For estimating the weak value A_w with*

precision ε and high probability, one needs $N^{(weak)} = O(|A_w|^2/\varepsilon^2\Delta_2(\phi, \psi))$ samples when using the standard weak measurement scheme with $\Delta_2(\phi, \psi) = |\langle\phi|\psi\rangle|^2$ being the probability of successful post-selection. Moreover, one needs $N^{(cycle-test)} = O(|A_w|^2/\varepsilon^2\Delta_2(\phi, \psi)^2)$ samples when using the cycle test.

We formally prove this result in Appendix A. Intuitively, the difference in the number of samples comes from the fact that the bound for the cycle test is constructed from the estimation of two quantities—a second- and a third-order invariant—while the standard weak measurement scheme directly estimates the weak value from the pointer’s position. Since to observe anomalous weak values in most relevant situations, and in particular in weak-value amplification schemes, the overlap Δ_2 needs to be close to zero,² this difference in sample complexity makes the protocol suboptimal. Therefore, one needs to look for specific cases of interest for which the cycle test may be more relevant. A clear example is provided by experimental situations in which one utilizes purely *imaginary* weak values [52–54]. In these cases, simply witnessing imaginarity boils down to observing imaginary third-order invariants related to the numerator of the weak value A_w , a task that, with high probability, requires at most only $O(d/\varepsilon^2)$ samples.

² However, note that weak values with a small imaginary part do not require small overlaps between the pre- and post-selections, but are also anomalous weak values. A simple example is the weak value of σ_x for a system pre-selected in $|z-\rangle$ and post-selected in $|y+\rangle$, which is $(\sigma_x)_w = -i$. A similar argument can be made when the real part of weak values lies slightly outside the interval determined by the spectrum of the operator.

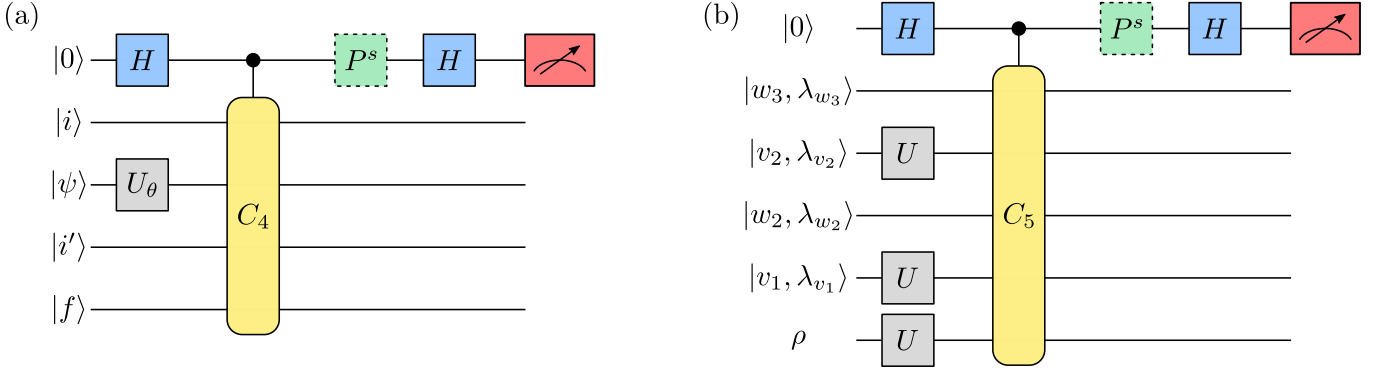


Figure 3. **Bargmann invariant circuits for measuring the extended Kirkwood-Dirac quasiprobability distributions behind (a) the post-selected quantum Fisher information and (b) the out-of-time-ordered correlator.** Part (a) shows how one can measure the post-selected quantum Fisher information using the cycle-test and applying a unitary operator $U_\theta = e^{-i\theta I}$ over the state $|\psi\rangle$ considered in the protocol. It is assumed to be possible to prepare, in parallel, states $|f\rangle$ associated with the post-selection and the eigenstates related to the operator I . Part (b) shows the protocol for estimating the out-of-time-ordered correlator from the related Bargmann invariants. A possibly scrambling unitary U is applied to ρ and to the projectors related to the eigenspaces of v and w defined by Π_v^V and Π_w^W , respectively. It is possible to avoid a backward-in-time evolution to estimate the OTOC, for any pair of observables V and W .

We have seen that circuits measuring Bargmann invariants can be used to measure weak values and KD distributions and that this information can also be used to perform quantum state tomography. However, we saw that some of these quantities can be extended in a way that involves a larger number of projectors and effectively needs higher-order invariants. Next, we discuss some applications that crucially require higher-order invariants and could be of interest to quantum information theory.

C. Applications for circuits measuring higher-order invariants

1. Post-selected quantum Fisher information

We have seen that the KD distribution can be extended, as described by Eq. (4), and that such constructions appeared in the literature, e.g., as an important quantity behind OTOCs or quantum advantage in post-selected metrology. In Fig. 3(a), we describe circuits specifically targeted to measuring such quantities. The Bargmann invariant circuit avoids post-selection and might be an interesting tool for measuring the post-selected quantum Fisher information in proof-of-principle experiments, such as the one performed in Ref. [40]. In Fig. 3(a), in order to measure the post-selected quantum Fisher information, we prepare the related quantum states of the eigenbasis $\{|i\rangle\}_{i \in \sigma(I)}$ of the observable I that slightly changes the state $|\psi\rangle$ via the action of $U_\theta = e^{i\theta I}$ parametrized by θ . The states $\{|f\rangle\}_f$ define the successful post-selection operator $F = \sum_f |f\rangle\langle f|$. The order in which those states are considered matters, and it is related to the order in the KD distribution presented in Eq. (6).

As discussed in Ref. [8, Supp. Note 2], imaginary

values of the post-selected quantum Fisher information do not contribute to metrological advantages since they cannot increase the second term of \mathcal{I}^{PS} , as described by Eq. (5). Hence, if one is only interested in witnessing the presence of the resource, namely negativity, one can use the circuit version of Fig. 3(a) with $s = 0$ (i.e., $P^s = \mathbb{1}$) to estimate the real part of the invariant.

2. Out-of-time-ordered correlators

In Fig. 3(b), we apply the cycle test to measure OTOCs. In Eq. (8), we may use the fact that U is unitary and that the Heisenberg and Schrödinger pictures are equivalent to re-write the Bargmann invariant defining the OTOC as

$$\begin{aligned} \text{Tr}(\Pi_{w_3}^{W(t)} \Pi_{v_2}^V \Pi_{w_2}^{W(t)} \Pi_{v_1}^V \rho) &= \\ &= \text{Tr}(U^\dagger \Pi_{w_3}^W U \Pi_{v_2}^V U^\dagger \Pi_{w_2}^W U \Pi_{v_1}^V \rho) \\ &= \text{Tr}(\Pi_{w_3}^W U \Pi_{v_2}^V U^\dagger \Pi_{w_2}^W U \Pi_{v_1}^V U^\dagger U \rho U^\dagger) \\ &= \text{Tr}(\Pi_{w_3}^W \mathcal{U}(\Pi_{v_2}^V) \Pi_{w_2}^W \mathcal{U}(\Pi_{v_1}^V) \mathcal{U}(\rho)), \end{aligned} \quad (16)$$

where $\mathcal{U}(\cdot) := U(\cdot)U^\dagger$ is the dynamical evolution in the Schrödinger picture. This allows us to have the cycle test that evaluates the OTOC without the need for applying a backward-in-time evolution U^\dagger . As compared with the protocols for estimating OTOCs reported in Ref. [4], not only does the cycle test avoid backward-in-time evolution, but also the auxiliary qubit does not need to remain coherent during the scrambling dynamics. The protocol estimates the extended KD distribution behind the OTOC in either its coarse-grained version or the fine-grained description of Eq. (11), which carries nonclassical information that brings further relevant tools to the analysis of the scrambling dynamics [9, 10].

These observations place the cycle test as an interesting new paradigm for estimating OTOCs, in comparison with all protocols reported in Ref. [4, Table I, pg. 12]. Two important drawbacks of this protocol are the fact that it requires quantum processing of information of possibly many degrees of freedom in parallel, together with the necessary assumption that one is capable of preparing the states associated with the eigenprojections II. Under the assumption that these are possible, Fig. 3(b) shows how to measure the quasiprobability distribution behind the OTOC described by Eq. (11).

A similar research direction was pursued in Ref. [55], where the authors analyzed when indirect metrological inference can be replaced by direct measurement processes, focusing on the Hadamard test. Our approach allows us to make claims that are similar in nature. For instance, Bargmann invariants can *also* be used to directly measure OTOCs, as we have seen.

3. Estimating the spectrum

So far, all quantities have depicted some relational aspect among different states in a set. Interestingly, cycle test circuits can also be used to estimate quantities associated with a single quantum state. In this section, we will consider one application of this idea, involving the estimation of the spectrum $\sigma(\rho)$ of a given mixed state ρ , an experimental task relevant for, e.g., quantifying coherence [56] or entanglement [57, 58] using resource theory monotones. For instance, learning the largest eigenvalue directly sets bounds on the entanglement between two parties as measured by the von Neumann entropy. Moreover, learning $\text{Tr}(\rho \dots \rho) \equiv \text{Tr}(\rho^n)$ can be used to directly estimate the Rényi entropy of order $n \geq 2$, given by

$$S_n(\rho) := \frac{1}{1-n} \log(\text{Tr}(\rho^n)), \quad (17)$$

as already noticed in Refs. [12, 59]. It is also possible to calculate some coherence monotones using information about the spectrum of the state, such as the relative entropy of coherence,

$$\mathcal{C}_{re}(\rho) := S(\rho_{diag}) - S(\rho), \quad (18)$$

where $S(\rho)$ is the von Neumann entropy and $\rho_{diag} = \sum_i \langle i | \rho | i \rangle |i\rangle\langle i|$, for the fixed reference basis $\{|i\rangle\}_i$ in the standard treatment of quantum coherence as a resource [56, 60].

It is possible to learn the spectrum $\sigma(\rho)$ from measurements of the quantities $\{\text{Tr}(\rho^n)\}_{n=1}^d$ with procedures that have been proposed using visibility-based quantum algorithms [61–64], via similar implementations of the cycle operator [12, 65], or using random measurements [66]. In Fig. 5, we describe the cycle test circuit that estimates $\text{Tr}(\rho^n)$ for any $n \in \mathbb{N}$. We consider a single auxiliary qubit and n Fredkin gates over n copies of the state ρ . This proposal is not optimal in the number

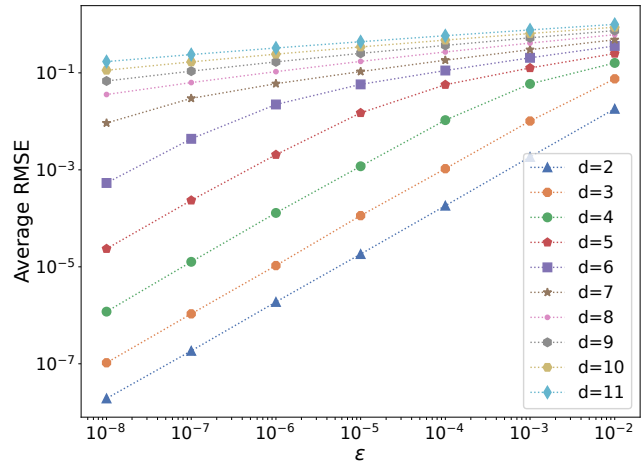


Figure 4. **Average root-mean-squared error (RMSE) of the estimate for the real part of the eigenvalues of random mixed states, under Gaussian noise ϵ .** We start from a data set of exact values of $\Delta_n := \text{Tr}(\rho^n)$, $\{\widehat{\Delta_n}\}_{n=2}^d$, introduce Gaussian noise with standard deviation ϵ , and plot the average root-mean-squared error (RMSE) of the estimated eigenvalues under noise. The spectrum reconstruction uses the Faddeev–LeVerrier algorithm based on Newton’s identities, and the average RMSE is over 5000 samples, each used to generate 1000 noisy samples. We use the Ginibre random ensemble of mixed states of rank larger than one, employing the algorithm introduced in Ref. [70].

of gates, however. In Refs. [11, 12], families of circuits were proposed with either log-depth or constant-depth. Yet, we observe that this advantage in depth is gained at the cost of an increase in space, as the proposals require the preparation of auxiliary multi-party Greenberger–Horne–Zeilinger (GHZ) states [67].

The Faddeev–LeVerrier algorithm, which uses the Newton identities [68, Chapter 3], allows us to compute the characteristic polynomial of the density matrix from the quantities $\{\text{Tr}(\rho^n)\}_{n=1}^d$. The eigenvalues are then obtained by finding the roots of the characteristic equation. We provide code for this computation, as well as supporting information, in the repository [69], where we present these ideas with an experimentally-friendly approach. This algorithm has some limitations, associated with finding the roots of the characteristic polynomial. As the dimension of the system increases, the coefficients of lower-degree monomials decrease, making them prone to numerical inaccuracies. We find that, for dimensions greater than 9, the predicted roots have an imaginary part bigger than 10^{-8} . This imaginary part appears due to numerical inaccuracies, and it is independent of statistical or experimental noise. Therefore, it does not affect the error in the real part of the predicted eigenvalues, and we may simply discard the imaginary part of the results. Appendix B presents a thorough study of this behavior.

In real experiments, noisy data will distort the predictions of the algorithm. In Fig. 4, we study the aggregated

root-mean-squared error (RMSE) of the real part of the eigenvalues of random mixed density matrices considering different amounts of noise in the experimental data. Given the traces of a random density matrix, we generate their noisy version by adding Gaussian noise with standard deviation ε to each one. In total, we generate $5 \cdot 10^4$ random density matrices from the Ginibre ensemble [70], each spawning 1000 different noisy versions of it. Since this error includes the estimation of the entire spectrum, it is expected that higher dimensions incur a high RMSE even for small ε . Expected errors in experimental realizations, i.e., errors of $\varepsilon \sim 10^{-3}$ would allow us to estimate the entire spectrum for dimensions 3 or 4 with good accuracy. A lower error ε in the experimental data could be attainable by increasing the number of samples. It is important to note that our numerical analysis only included statistical errors. More detailed knowledge of specific experimental implementations would be required for a more realistic error analysis.

A simpler task involves learning the largest eigenvalue with high precision. This task should give better results as the highest degree coefficients of the characteristic polynomial have a greater size than those of lower degrees and will be less affected by noise. We study the scaling of the error in the estimation of the largest eigenvalue in Appendix B. As expected, higher dimensional systems can be studied. For instance, for an experimental error of $\varepsilon = 10^{-4}$, the average RMSE is around 5×10^{-3} for dimension 6. However, measuring the complete set of traces for estimating the largest eigenvalue is not an optimal procedure. While the coefficients of higher-degree monomials of the polynomial require traces of lower orders in powers of the density matrix, coefficients of lower degrees require traces of higher orders. As these traces require a more complex circuit, they will also be noisier. A sensible alternative to computing the largest eigenvalue is truncating the polynomial to a certain lower degree k [59]. That is, computing the polynomial coefficients of higher degrees using traces of lower powers of ρ $\{\text{Tr}(\rho^2), \dots, \text{Tr}(\rho^{d-k})\}$. In this approximation, the traces that are more difficult to measure are not taken into account, as they contribute less.

Oddly enough, estimating the spectrum of ρ from $\{\text{Tr}(\rho^n)\}_{n=1}^d$ for $d > 2$ has not, to the best of our knowledge, received any attention from experimental investigations yet, even though one can show that the required number of samples is optimal.

Lemma 2. *The number of samples needed to estimate $\{\text{Tr}(\rho^n)\}_{n=1}^d$ up to precision ε in all quantities with high probability is $N = \tilde{O}(d^2/\varepsilon^2)$ with the cycle test. The number of measurements needed over auxiliary qubits is $\tilde{O}(d/\varepsilon^2)$.*

We prove this lemma in Appendix B. The protocol of Ref. [12] improves this sample complexity by logarithm factors, obtaining that order $O(d^2/\varepsilon^2)$ samples are needed with high probability. One can learn the spectrum of a given state ρ using an optimal number of sam-

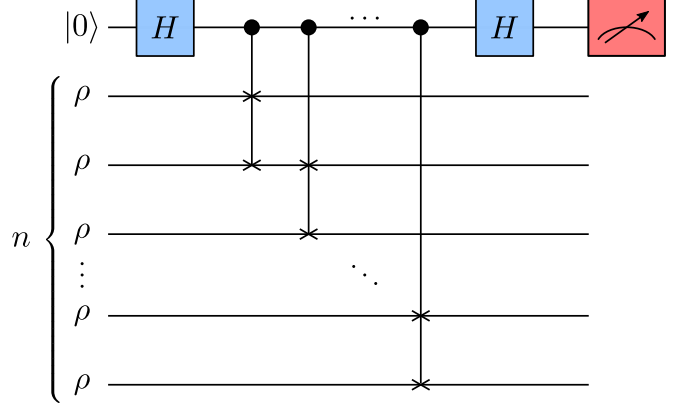


Figure 5. **Circuit for measuring $\text{Tr}(\rho^n)$.** The input consists of n copies of a d -dimensional state ρ . Measurements of $\text{Tr}(\rho^n)$ for $n = 1, 2, \dots, d$ gives us the spectrum of ρ , via the Newton identities.

ples and measurements using the cycle test circuits described in this work or those described in Ref. [12]. The best bounds on the number of samples needed to estimate the spectrum $\sigma(\rho)$ for d -dimensional mixed states ρ were first rigorously obtained in Refs. [71, 72] with the use of the empirical Young diagram (EYD) algorithm, later connected with complexity theory arguments [73, 74], and formally used to show that the same sample complexity is optimal for full state tomography [49, 75–77].

Some important differences between the two methods for learning the spectrum—the EYD algorithm and the protocol described above—deserve to be mentioned. To implement the EYD algorithm, one needs to measure $\rho^{\otimes n}$ in the highly entangled Schur basis; and to obtain the spectrum with precision ε , one needs $n_{EYD} = O(d^2/\varepsilon^2)$. In terms of sample complexity, this is optimal: one requires $N = n_{EYD}$ copies of ρ , which is the optimal sample complexity—and the same as in our protocol, as stated before.

At first glance, the EYD algorithm may seem to be simpler, as it requires implementing only a single quantum circuit. Indeed, one should choose a large enough value of n_{EYD} , and then implement the Schur transform (mapping the Schur basis to the computational one) and measure the final state only for that fixed n_{EYD} . In contrast, our approach requires estimating $\text{Tr}(\rho^n)$ for $n = 1, \dots, d$, where every increment of n requires a slightly larger circuit. However, this “partition” of the algorithm into d quantum circuits holds a huge practical advantage. As is evident from the previous paragraph, the EYD algorithm requires a quantum computer that can reliably sustain a highly entangled state in a Hilbert space of dimension $d^{n_{EYD}}$. This dimension grows larger for smaller desired precision ε . Meanwhile, in our approach, the largest circuit requires a dimension d^d —which still grows large for higher values of d but does not depend on ε . Moreover, the gate complexity of the Schur transform is polynomial in both d and n_{EYD} [78], while the complexity of the cir-

cuit for measuring $\text{Tr}(\rho^n)$ only depends on n^3 . Thus, the gate complexity of our approach does not depend on ε and is generally much smaller when compared with EYD.

It should be noted that the authors of Ref. [79] overcome the issue of gate complexity by considering a specific experimental setup where the symmetry of the interaction Hamiltonian is utilized to implement the Schur transform efficiently⁴.

We proceed to study simple setups for which it is possible to witness the nonclassicality of Bargmann invariants, briefly pointing out how nonclassicality, in the sense of negativity or imaginarity, is related to a particular notion of coherence.

IV. MINIMAL EXPERIMENTAL CONDITIONS FOR WITNESSING NONCLASSICALITY

Most of the quantities just discussed capture the community's interest because they present features that are puzzling to be described classically—specifically, negative and imaginary values. Given that the algorithms discussed in this work are capable of assessing these quantities, we are now interested in studying minimal experimental setups to witness nonclassicality. For that, let us first discuss how the negativity or imaginarity of Bargmann invariants can be understood as witnesses of quantum coherence.

Consider a given tuple of states $\underline{\rho} \equiv (\rho_i)_{i=1}^n$ and suppose that those states are all diagonal with respect to some reference basis, meaning that there exists a unitary U such that $U\rho_i U^\dagger$ are diagonal. As was described in Refs. [11, 80, 81] the assumption of set-incoherence—or equivalently, pairwise commutativity of all elements of $\underline{\rho}$ —imposes restrictions over tuples of Bargmann invariants forming convex polytopes of probabilistic correlations. Assuming that $\underline{\rho}$ can be diagonal with respect to some basis, any Bargmann invariant takes the form

$$\Delta_n(\underline{\rho}) = \sum_k p_k^{(1)} \dots p_k^{(n)}, \quad (19)$$

where $\underline{\rho} \ni \rho^{(k)} = \text{diag}(p_1^{(k)}, \dots, p_d^{(k)})$ and $d = \dim(\mathcal{H})$. This implies that $\Delta_n(\underline{\rho})$ can be understood as the probability that, upon measuring all n states with the reference observable that diagonalizes $\underline{\rho}$, they all return equal outcomes. Clearly, negative or imaginary values contradict such a possibility.

This property was analyzed in Ref. [11], but we make the trivial, albeit important, connection between set co-

herence, imaginarity, and negativity that is attributed to those quantities:

Lemma 3 (Adapted from results of Ref. [11]). *Negativity or imaginarity of weak values A_w witness the coherence of the set of states $\{|a\rangle\}_{a \in \sigma(A)} \cup \{|\phi\rangle, |\psi\rangle\}$ corresponding to the pre- and post-selection and the eigenstates of observable A . Negativity or imaginarity of KD distributions $\xi(\rho|i, f)$ correspond to witnesses of the coherence of the set of states $\{\rho\} \cup \{|i\rangle\}_i \cup \{|f\rangle\}_f$. The same holds for any of the extended KD distributions.*

This leads to a direct corollary for the results in Ref. [8], as we now see. The important aspect of \mathcal{I}^{ps} for metrology is that it can be larger than what might be achieved without post-selection for a generic prepare-and-measure experiment, $\max_\rho \mathcal{I}$. These larger values for the quantum Fisher information were called *anomalous* in Ref. [8]. Any value of \mathcal{I}^{ps} that is larger than an optimal prepare-and-measure estimation without post-selection requires negative values of the extended KD distribution from Eq. (6). Because negativity of this extended KD distribution is necessary, we obtain:

Corollary 4. *Coherence for a set of states is a necessary, but not a sufficient, resource for anomalous quantum Fisher information in post-selected metrology.*

The analysis of Bargmann invariants for diagonal states sheds some light on the reason why negativity and imaginarity are notions of nonclassicality strictly tighter than set coherence or commutativity, as noticed in Ref. [82]. These conditions over Bargmann invariants are only two among *many* conditions that such quantities should satisfy in order to corroborate the assumptions connected to the classical probabilistic interpretation provided by Eq. (19). It is, therefore, immediate that negativity or imaginarity *alone* are incapable of capturing set coherence. To illustrate this point, consider the following triplet of states

$$\{|\psi_1\rangle, |\psi_2\rangle, |\psi_3\rangle\} := \left\{ |0\rangle, \frac{|0\rangle + \sqrt{3}|1\rangle}{2}, \frac{\sqrt{3}|0\rangle + |1\rangle}{2} \right\}.$$

These states have $\mathbb{R} \ni \Delta_3 = \frac{3}{8} > 0$, while being basis-independent set coherent, as can be seen from the fact that these states violate the coherence witness inequalities from Refs. [7, 80]. To be concrete, they violate the inequality $h = -\Delta_2(\psi_1, \psi_2) + \Delta_2(\psi_1, \psi_3) + \Delta_2(\psi_2, \psi_3) \leq 1$ since for these states $h = -1/4 + 3/4 + 3/4 = 5/4 > 1$. Later on, we will also discuss these two-state overlap inequalities in Eq. (25) in a different context. However, for a proof that these inequalities are witnesses of coherence, we refer the reader to the discussions presented in Refs. [7, 80].

In Refs. [82–85], the authors studied conditions for which non-zero phase-space points for the Bargmann invariants behind the KD distribution are sufficient to claim *some* negativity or imaginarity. It was shown that,

³ Or even better, achieving $\log(n)$, as shown in Ref. [11], or constant-depth, as shown in Ref. [12].

⁴ While acknowledging that some of the experimental aspects needed to implement the EYD algorithm “seem like a daunting task in practice” [79, pg. 3]

letting $n_I(\psi) := |\{i \in \sigma(I) : \langle i|\psi\rangle \neq 0\}|$ with $|\cdot|$ being the cardinality of the set, one obtains negativity or imaginarity when

$$n_I(\psi) + n_F(\psi) > d + 1, \quad (20)$$

where d is the dimension of the Hilbert space, under the assumption that $\langle i|f\rangle \neq 0$ for any i, f in the two bases of the KD phase space. In the case the two bases I, F are mutually unbiased, $|\psi\rangle$ will be classical, i.e., it will have KD phase real and non-negative, if and only if [85]

$$n_I(\psi)n_F(\psi) = d. \quad (21)$$

Note that, in both cases, one assumes a dimension of the physical system and, moreover, that in order to apply those results, one needs information about all the overlaps $\Delta_2(i, f), \Delta_2(i, \psi), \Delta_2(\psi, f)$, namely whether they are zero or not.

We can address the same question from a new perspective using the information provided by the two-state overlaps. Focusing on each triplet $|\psi\rangle, |i\rangle, |f\rangle$ for fixed i, f , we want to study if it is possible to witness negativity and imaginarity using only the value of the overlaps without assuming a specific Hilbert space dimension. We can, then, state the following impossibility result in this direction:

Theorem 5. *For any triplet of states $|\psi\rangle, |i\rangle, |f\rangle \in \mathcal{H}$, where \mathcal{H} is a finite-dimensional Hilbert space, and assuming knowledge about all pairwise overlaps $\Delta_2(i, \psi), \Delta_2(f, \psi)$, and $\Delta_2(i, f)$ only, it is impossible to perfectly discriminate between imaginary and real third-order Bargmann invariants, e.g., decide with certainty between $\text{Im}[\Delta_3(i, \psi, f)] = 0$ or $\text{Im}[\Delta_3(i, \psi, f)] \neq 0$. More broadly, every triplet of quantum two-state overlaps can be expressed using states with only real amplitudes. Moreover, provided that the third-order invariant is real, it is impossible to perfectly discriminate between positive and negative third-order Bargmann invariant, e.g., perfectly discriminate between $\Delta_3(i, \psi, f) > 0$ or $\Delta_3(i, \psi, f) < 0$.*

Proof. We show the first part of the result using two simple counterexamples. Letting the triplet of states $\{|0\rangle, |+\rangle, |i+\rangle\}$ for which $|i+\rangle = \frac{1}{\sqrt{2}}(|0\rangle + i|1\rangle)$ we have all overlaps equal to $1/2$ while $\text{Im}[\Delta_3] \neq 0$. We now construct a triplet of states with all overlaps equal to $1/2$, but that comes from states with only real amplitudes. The simplest example is the triplet of maximally mixed qubits, $\mathbb{1}/2$. Moreover, even if one restricts to pure states, it does not resolve the issue because the following states form a real triplet with overlaps $1/2$:

$$\left\{ \frac{|0\rangle + |1\rangle}{\sqrt{2}}, \frac{|1\rangle + |2\rangle}{\sqrt{2}}, \frac{|0\rangle + |2\rangle}{\sqrt{2}} \right\}. \quad (22)$$

We now argue that triplets of states with real amplitudes can reach any value for the three overlaps. If we consider the body of all possible overlap triples $(\Delta_2(i, \psi), \Delta_2(f, \psi), \Delta_2(i, f))$ for any triplet of quantum

states in any dimension this forms the quantum set described in Ref. [80]. It was shown there that all maximal violations can be reached with overlaps described by real-amplitude states only. Since the set is convex, it is possible to describe any triplet of overlaps using convex combinations of overlaps realized by real-amplitude quantum states, and, therefore, one cannot conclude if these states are imaginary just from the information on overlaps.

Then, it remains to be shown that the discrimination task remains impossible in the case of distinguishing between positive and negative real third-order invariants. If we choose the tuple of states

$$\left\{ |0\rangle, \frac{|0\rangle + \sqrt{3}|1\rangle}{2}, \frac{|0\rangle - \sqrt{3}|1\rangle}{2} \right\}, \quad (23)$$

all three overlaps equal $1/4$, while $\Delta_3 = -1/8 < 0$. If, instead, we choose the triplet of overlaps

$$\left\{ |0\rangle, \frac{|0\rangle + \sqrt{3}|1\rangle}{2}, \frac{3|0\rangle + \sqrt{3}|1\rangle + \sqrt{24}|2\rangle}{6} \right\}, \quad (24)$$

all overlaps, once more, equal $1/4$, while $\Delta_3 = +1/8 > 0$. This concludes the proof. \square

In words, this theorem shows that overlaps alone cannot witness negativity or imaginarity of third-order invariants. One needs more information, in general, provided by the Hilbert space dimension. Other possibilities might be to analyze case by case, depending on the form of the states that can be generated by a particular device or relaxing the information that can be obtained by overlaps.

Let us now see how information on purity or Hilbert-space dimension can be used to supplement the overlap information and allow for better discrimination of non-classicality. For instance, three *pure* single-qubit states that have pairwise overlaps of $1/2$ must have an imaginary third-order invariant. In the following, we use overlap inequalities studied in Refs. [80, 81, 86] as witnesses of basis-independent coherence. This allows us to obtain a more general result for three single-qubit states with real amplitudes.

Let $|i\rangle, |f\rangle, |\psi\rangle$ be one-qubit states with real amplitudes with respect to some basis. As we will see, then no two of the following inequalities can hold,

$$\begin{aligned} \Delta_3(i, f, \psi) &< 0, \\ +\Delta_2(i, f) + \Delta_2(i, \psi) - \Delta_2(f, \psi) &> 1, \\ +\Delta_2(i, f) - \Delta_2(i, \psi) + \Delta_2(f, \psi) &> 1, \\ -\Delta_2(i, f) + \Delta_2(i, \psi) + \Delta_2(f, \psi) &> 1. \end{aligned} \quad (25)$$

For any such triplet, there exists a unitary that sends them into the rebit subspace. This implies that we can parametrize these states in the following way;

$$\begin{aligned} |\psi\rangle &= |0\rangle \\ |i\rangle &= \cos(\theta)|0\rangle + \sin(\theta)|1\rangle \\ |f\rangle &= \cos(\phi)|0\rangle + \sin(\phi)|1\rangle. \end{aligned} \quad (26)$$

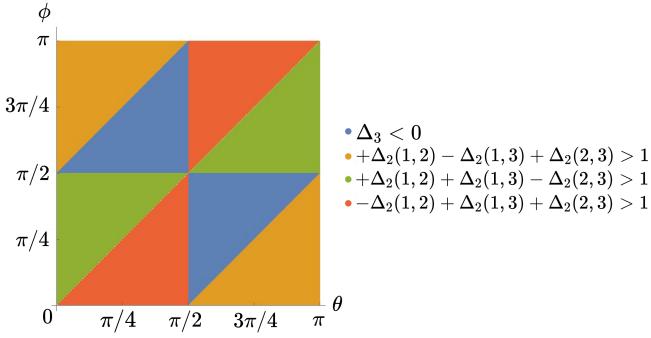


Figure 6. **Negativity of third-order invariants from measurements of overlaps only.** For real-amplitude one-qubit states, we show a complementarity relation between negativity of third-order invariants and overlap inequalities. Here we use the notation $\Delta_2(1,2) = |\langle\psi_1|\psi_2\rangle|^2$ and $\Delta_3 = \langle\psi_1|\psi_2\rangle\langle\psi_2|\psi_3\rangle\langle\psi_3|\psi_1\rangle$.

with $\theta, \phi \in [0, \pi]$ being sufficient to capture all possible values, implying that $\Delta_3(i, f, \psi) = \cos(\theta - \psi)\cos(\theta)\cos(\phi)$, $\Delta_2(i, \psi) = \cos^2(\theta)$, $\Delta_2(f, \psi) = \cos^2(\phi)$, and $\Delta_2(i, f) = \cos^2(\theta - \phi)$. The images over θ and ϕ for the relevant functions satisfying the inequalities are plotted in Fig. 6, where we can see that each value of θ and ϕ defining a triplet satisfies one, and only one inequality.

This insight allows us to search for similar results, converging to the following lemma:

Lemma 6. *Let $\{|\psi_i\rangle\}_{i=1}^3$ be any triplet of pure states real with respect to some basis for a finite-dimensional Hilbert space \mathcal{H} of dimension d . Let $\Delta_2(i, j) = |\langle\psi_i|\psi_j\rangle|^2$ and $\Delta_3(i, j, k) = \langle\psi_i|\psi_j\rangle\langle\psi_j|\psi_k\rangle\langle\psi_k|\psi_i\rangle \equiv \Delta_3$ for brevity. Then, we have that*

$$\begin{aligned} \Delta_2(1, 2) + \Delta_2(1, 3) - \Delta_2(2, 3) &> 1 \Rightarrow \Delta_3 > 0 \\ \Delta_2(1, 2) - \Delta_2(1, 3) + \Delta_2(2, 3) &> 1 \Rightarrow \Delta_3 > 0 \\ -\Delta_2(1, 2) + \Delta_2(1, 3) + \Delta_2(2, 3) &> 1 \Rightarrow \Delta_3 > 0. \end{aligned} \quad (27)$$

In the case $d = 2$, the other direction holds as well, i.e., if all overlap inequalities described above are strictly less than 1, we get that $\Delta_3 < 0$.

We prove this lemma in Appendix C. The part of the lemma regarding dimension $d = 2$ was already shown by our previous argument and is depicted in Fig. 6. Overlaps provide a simple test for when the third-order invariants are positive, in which case it might simplify the search for negativity.

These results suggest a clear-cut, step-by-step experimental procedure to witness negativity or imaginarity of KD phase space:

1. Measure all overlaps $\Delta_2(i, f), \Delta_2(\rho, f), \Delta_2(i, \psi)$. Use the results from Refs. [82, 83] to determine, based only on information on how many of these overlaps are non-zero, whether it is possible to witness nonclassicality of third-order Bargmann invariants.

2. Let us assume the test above was inconclusive. Next, we consider the third-order invariant of each triplet of states $\{|i\rangle, |f\rangle, |\psi\rangle\}$. Measure the imaginary part of the third-order invariants $\text{Im}[\xi(\psi|i, f)] = \text{Im}[\Delta_3(\psi, i, f)]$ using the circuits we have presented. In case it is non-zero, we witness nonclassicality as wanted; otherwise, from the results of Ref. [11] we know that there exists a basis representation of this triplet of vectors using only real amplitudes.

3. If the tests so far were inconclusive, we have a purely real-valued third-order invariant. The triplet of overlaps can provide information regarding the negativity of the third-order invariants, as described in the statement of lemma 6.
4. Lastly, we measure the real part of the invariant of those selected triplets that could still have a negative invariant.

Lemma 6 provides only a necessary condition for understanding if one can witness negativity of third-order invariants. There might exist more fine-tuned examples depending on the states that can be generated by particular devices or knowledge of the dimension that can be analyzed case by case, as already noticed in Fig. 6.

V. DISCUSSION AND FUTURE DIRECTIONS

In this work, we have explored two complementary approaches to a better understanding of nonclassicality in quantum information processing. The first approach is more practical and application-focused, where we show simple quantum circuits that can be used to estimate various quantities of fundamental interest by measuring multivariate traces known as Bargmann invariants. Specifically, we have described circuits to experimentally estimate the spectrum of any mixed quantum state, weak values, KD quasiprobability distribution, post-selected quantum Fisher information, and OTOCs. The second approach is more foundational, and investigates conditions for the nonclassicality of these quantities, understood as negativity and imaginarity, relating it to the presence of a recently introduced quantum resource termed set coherence, which acknowledges coherence as a basis-independent, relational property of a set of states.

These results bring proof-of-principle tests of the nonclassicality of quantum theory—a vital resource for information processing—closer to current experimental capabilities. Indirect measurements of unitary invariants up to fourth order have been made in different platforms [87–89]. We believe that the unified view of nonclassicality we discussed here may boost the interest in a systematic exploration of nonclassicality witnessed and quantified by unitary invariants. Moreover, the connection of coherence theory with all the above quantities motivates not only the construction of a formal resource theory based

on Bargmann invariants but also the experimental investigation of coherence for higher dimensional systems through the lens of formal monotones.

The relationship between Bargmann invariants and KD distributions could bring quantitative understanding to other problems of interest. For instance, the non-classicality of Bargmann invariants understood as witnesses of coherence may clarify the connection between the nonclassicality of OTOCs and scrambling of information [9] for quantum computation. This new view could lead to more robust and rigorous ways of benchmarking the scrambling of information against decoherence that goes beyond numerical evidence [90]. Another interesting point to notice is that the tools described in Ref. [11] and further developed here clarify the understanding of when it is indeed *crucial* to experimentally estimate higher-order invariants in extended KD distributions. It would be interesting to characterize the minimum cardinality and/or degree of sets of Bargmann invariants that are necessary for quantifying nonclassicality in particular applications.

As a final technical remark, even though some of the results regarding the use of the quantities $\text{Tr}(\rho^n)$ for $n = 2, \dots, d$ have previously appeared in the literature, we stress that our sample complexity analysis and numerical experiments have shown concrete benefits of learning the spectrum using the higher-order Bargmann invariants. Interesting future work in this direction could involve experimentally probing $\text{Tr}(\rho^n)$ for small $n = 2, 3, 4$, using the information to estimate the spectrum of density matrices.

Given the foundational importance of KD distributions and weak values, we expect that our unified framework based on measurements of Bargmann invariants will provide both theoretical insight and practical recipes for experimental implementations of the many applications we analyze here.

ACKNOWLEDGMENTS

We thank the International Iberian Nanotechnology Laboratory (INL) and the Bar-Ilan Institute of Nanotechnology and Advanced Materials (BINA) for their support, which was instrumental in kick-starting this collaboration. RW and ARM acknowledge support from FCT – Fundação para a Ciência e a Tecnologia (Portugal) through PhD Grants SFRH/BD/151199/2021 and SFRH/BD/151453/2021, respectively. RSB and EFG also acknowledge support from FCT, CECINST/00062/2018. ILP acknowledges support from the ERC Advanced Grant FLQuant. The work of INL-based authors (RW, ARM, RSB, EFG) was supported by the Digital Horizon Europe project FoQaCiA, GA no. 101070558. EC was supported by the Israeli Innovation Authority under Project 73795 and the Eureka project, by Elta Systems Ltd., by the Pazy Foundation, by the Israeli Ministry of Science and Technology, and by the Quantum Science and Technology Program of the Israeli Council of Higher Education.

[1] Y. Aharonov, D. Z. Albert, and L. Vaidman, How the result of a measurement of a component of the spin of a spin-1/2 particle can turn out to be 100, *Phys. Rev. Lett.* **60**, 1351 (1988).

[2] J. G. Kirkwood, Quantum statistics of almost classical assemblies, *Phys. Rev.* **44**, 31 (1933).

[3] P. A. M. Dirac, On the analogy between classical and quantum mechanics, *Rev. Mod. Phys.* **17**, 195 (1945).

[4] N. Y. Halpern, B. Swingle, and J. Dressel, Quasiprobability behind the out-of-time-ordered correlator, *Phys. Rev. A* **97**, 042105 (2018).

[5] M. Lostaglio, A. Belenchia, A. Levy, S. Hernández-Gómez, N. Fabbri, and S. Gherardini, *Kirkwood-Dirac quasiprobability approach to quantum fluctuations: Theoretical and experimental perspectives*, arXiv:2206.11783 [quant-ph] (2022).

[6] E. Cohen and E. Pollak, Determination of weak values of quantum operators using only strong measurements, *Phys. Rev. A* **98**, 042112 (2018).

[7] T. Giordani, C. Esposito, F. Hoch, G. Carvacho, D. J. Brod, E. F. Galvão, N. Spagnolo, and F. Sciarrino, Witnesses of coherence and dimension from multiphoton indistinguishability tests, *Phys. Rev. Res.* **3**, 023031 (2021).

[8] D. R. M. Arvidsson-Shukur, N. Y. Halpern, H. V. Lepage, A. A. Lasek, C. H. W. Barnes, and S. Lloyd, Quantum advantage in postselected metrology, *Nat. Comm.* **11**, 3775 (2020).

[9] J. R. González Alonso, N. Yunger Halpern, and J. Dressel, Out-of-time-ordered-correlator quasiprobabilities robustly witness scrambling, *Phys. Rev. Lett.* **122**, 040404 (2019).

[10] J. R. G. Alonso, N. Shammah, S. Ahmed, F. Nori, and J. Dressel, *Diagnosing quantum chaos with out-of-time-ordered-correlator quasiprobability in the kicked-top model*, arXiv:2201.08175 [quant-ph] (2022).

[11] M. Oszmaniec, D. J. Brod, and E. F. Galvão, *Measuring relational information between quantum states, and applications*, arXiv:2109.10006 [quant-ph] (2021).

[12] Y. Quek, M. M. Wilde, and E. Kaur, *Multivariate trace estimation in constant quantum depth*, arXiv:2206.15405 [quant-ph] (2022).

[13] L. Vaidman, Weak value controversy, *Philos. Trans. R. Soc. A* **375**, 20160395 (2017).

[14] M. F. Pusey, Anomalous weak values are proofs of contextuality, *Phys. Rev. Lett.* **113**, 200401 (2014).

[15] R. Kunjwal, M. Lostaglio, and M. F. Pusey, Anomalous weak values and contextuality: robustness, tightness, and imaginary parts, *Phys. Rev. A* **100**, 042116 (2019).

[16] E. Rebufello, F. Piacentini, A. Avella, M. A. d. Souza, M. Gramegna, J. Dziewior, E. Cohen, L. Vaidman, I. P. Degiovanni, and M. Genovese, Anomalous weak values via a single photon detection, *Light Sci. Appl.* **10**, 106

(2021).

[17] P. B. Dixon, D. J. Starling, A. N. Jordan, and J. C. Howell, Ultrasensitive beam deflection measurement via interferometric weak value amplification, *Phys. Rev. Lett.* **102**, 173601 (2009).

[18] M. D. Turner, C. A. Hagedorn, S. Schlamminger, and J. H. Gundlach, Picoradian deflection measurement with an interferometric quasi-autocollimator using weak value amplification, *Opt. Lett.* **36**, 1479 (2011).

[19] Y. Susa, Y. Shikano, and A. Hosoya, Optimal probe wave function of weak-value amplification, *Phys. Rev. A* **85**, 052110 (2012).

[20] J. Dressel, K. Lyons, A. N. Jordan, T. M. Graham, and P. G. Kwiat, Strengthening weak-value amplification with recycled photons, *Phys. Rev. A* **88**, 023821 (2013).

[21] A. N. Jordan, J. Martínez-Rincón, and J. C. Howell, Technical advantages for weak-value amplification: when less is more, *Phys. Rev. X* **4**, 011031 (2014).

[22] S. Pang, J. Dressel, and T. A. Brun, Entanglement-assisted weak value amplification, *Phys. Rev. Lett.* **113**, 030401 (2014).

[23] G. B. Alves, B. Escher, R. L. de Matos Filho, N. Zagury, and L. Davidovich, Weak-value amplification as an optimal metrological protocol, *Phys. Rev. A* **91**, 062107 (2015).

[24] J. Harris, R. W. Boyd, and J. S. Lundeen, Weak value amplification can outperform conventional measurement in the presence of detector saturation, *Phys. Rev. Lett.* **118**, 070802 (2017).

[25] M. Pfender, P. Wang, H. Sumiya, S. Onoda, W. Yang, D. B. R. Dasari, P. Neumann, X.-Y. Pan, J. Isoya, R.-B. Liu, et al., High-resolution spectroscopy of single nuclear spins via sequential weak measurements, *Nat. Commun.* **10**, 594 (2019).

[26] K. S. Cujia, J. M. Boss, K. Herb, J. Zopes, and C. L. Degen, Tracking the precession of single nuclear spins by weak measurements, *Nature* **571**, 230 (2019).

[27] S.-Z. Fang, H.-T. Tan, G.-X. Li, and Q.-L. Wu, Weak value amplification for angular velocity measurements, *Appl. Opt.* **60**, 4335 (2021).

[28] J.-H. Huang, X.-Y. Duan, and X.-Y. Hu, Amplification of rotation velocity using weak measurements in Sagnac's interferometer, *Eur. Phys. J. D* **75**, 114 (2021).

[29] I. L. Paiva, R. Lenny, and E. Cohen, Geometric phases and the Sagnac effect: Foundational aspects and sensing applications, *Adv. Quantum Tech.* **5**, 2100121 (2022).

[30] H. Cramér, **Mathematical methods of statistics** (Princeton University Press, Princeton, NJ, 1946).

[31] C. R. Rao, Information and the accuracy attainable in the estimation of statistical parameters, *Bull. Calcutta Math. Soc.* **37**, 81 (1945).

[32] A. Ly, M. Marsman, J. Verhagen, R. Grasman, and E.-J. Wagenmakers, A tutorial on Fisher information, *J. Math. Psychol.* **80**, 40 (2017).

[33] J. Liu, H. Yuan, X.-M. Lu, and X. Wang, Quantum Fisher information matrix and multiparameter estimation, *J. Phys. A* **53**, 023001 (2019).

[34] M. G. A. Paris, Quantum estimation for quantum technology, *Int. J. Quantum Inf.* **7**, 125 (2009).

[35] J. Preskill, Quantum computing in the NISQ era and beyond, *Quantum* **2**, 79 (2018).

[36] K. Bharti, A. Cervera-Lierta, T. H. Kyaw, T. Haug, S. Alperin-Lea, A. Anand, M. Degroote, H. Heimonen, J. S. Kottmann, T. Menke, W.-K. Mok, S. Sim, L.-C. Kwek, and A. Aspuru-Guzik, Noisy intermediate-scale quantum algorithms, *Rev. Mod. Phys.* **94**, 015004 (2022).

[37] K. Bharti, Fisher information: A crucial tool for NISQ research, *Quantum Views* **5**, 61 (2021).

[38] J. J. Meyer, Fisher information in noisy intermediate-scale quantum applications, *Quantum* **5**, 539 (2021).

[39] X. Zhang, X.-M. Lu, J. Liu, W. Ding, and X. Wang, Direct measurement of quantum Fisher information, *Phys. Rev. A* **107**, 012414 (2023).

[40] N. Lupu-Gladstein, Y. B. Yilmaz, D. R. Arvidsson-Shukur, A. Brodutch, A. O. Pang, A. M. Steinberg, and N. Y. Halpern, Negative quasiprobabilities enhance phase estimation in quantum-optics experiment, *Phys. Rev. Lett.* **128**, 220504 (2022).

[41] S. Das, S. Modak, and M. N. Bera, *Bounding quantum advantages in postselected metrology*, arXiv:2108.09220 [quant-ph] (2021).

[42] A. Wiggins, Mathematics and computation, in **Mathematics and Computation** (Princeton University Press, Princeton, NJ, 2019).

[43] S. Designolle, R. Uola, K. Luoma, and N. Brunner, Set coherence: Basis-independent quantification of quantum coherence, *Phys. Rev. Lett.* **126**, 220404 (2021).

[44] L. M. Johansen, Quantum theory of successive projective measurements, *Phys. Rev. A* **76**, 012119 (2007).

[45] M. A. Nielsen and I. Chuang, **Quantum computation and quantum information** (Cambridge University Press, Cambridge, UK, 2000).

[46] S. T. Flammia, D. Gross, Y.-K. Liu, and J. Eisert, Quantum tomography via compressed sensing: error bounds, sample complexity and efficient estimators, *New J. Phys.* **14**, 095022 (2012).

[47] W. Hoeffding, Probability inequalities for sums of bounded random variables, *J. Am. Stat. Assoc.* **58**, 13 (1963).

[48] S. Shalev-Shwartz and S. Ben-David, **Understanding machine learning: From theory to algorithms** (Cambridge University Press, New York, NY, 2014).

[49] S. Chen, B. Huang, J. Li, A. Liu, and M. Sellke, *Tight bounds for state tomography with incoherent measurements*, arXiv:2206.05265 [quant-ph] (2022).

[50] L. M. Johansen, Reconstructing weak values without weak measurements, *Phys. Lett. A* **366**, 374 (2007).

[51] G. Vallone and D. Dequal, Strong measurements give a better direct measurement of the quantum wave function, *Phys. Rev. Lett.* **116**, 040502 (2016).

[52] N. Brunner and C. Simon, Measuring small longitudinal phase shifts: weak measurements or standard interferometry?, *Phys. Rev. Lett.* **105**, 010405 (2010).

[53] C.-F. Li, X.-Y. Xu, J.-S. Tang, J.-S. Xu, and G.-C. Guo, Ultrasensitive phase estimation with white light, *Phys. Rev. A* **83**, 044102 (2011).

[54] J. Dressel and A. N. Jordan, Significance of the imaginary part of the weak value, *Phys. Rev. A* **85**, 012107 (2012).

[55] K. Mitarai and K. Fujii, Methodology for replacing indirect measurements with direct measurements, *Phys. Rev. Res.* **1**, 013006 (2019).

[56] A. Streltsov, G. Adesso, and M. B. Plenio, Colloquium: Quantum coherence as a resource, *Rev. Mod. Phys.* **89**, 041003 (2017).

[57] V. Vedral, M. B. Plenio, M. A. Rippin, and P. L. Knight, Quantifying entanglement, *Phys. Rev. Lett.* **78**, 2275 (1997).

[58] R. Horodecki, P. Horodecki, M. Horodecki, and

K. Horodecki, Quantum entanglement, *Rev. Mod. Phys.* **81**, 865 (2009).

[59] Y. Subaşı, L. Cincio, and P. J. Coles, Entanglement spectroscopy with a depth-two quantum circuit, *J. Phys. A* **52**, 044001 (2019).

[60] J. Åberg, Quantifying superposition, arXiv:quant-ph/0612146 (2006).

[61] A. K. Ekert, C. M. Alves, D. K. L. Oi, M. Horodecki, P. Horodecki, and L. C. Kwek, Direct estimations of linear and nonlinear functionals of a quantum state, *Phys. Rev. Lett.* **88**, 217901 (2002).

[62] C. M. Alves, P. Horodecki, D. K. L. Oi, L. C. Kwek, and A. K. Ekert, Direct estimation of functionals of density operators by local operations and classical communication, *Phys. Rev. A* **68**, 032306 (2003).

[63] P. Horodecki, From limits of quantum operations to multicopy entanglement witnesses and state-spectrum estimation, *Phys. Rev. A* **68**, 052101 (2003).

[64] P. Horodecki and A. Ekert, Method for direct detection of quantum entanglement, *Phys. Rev. Lett.* **89**, 127902 (2002).

[65] T. Tanaka, Y. Ota, M. Kanazawa, G. Kimura, H. Nakazato, and F. Nori, Determining eigenvalues of a density matrix with minimal information in a single experimental setting, *Phys. Rev. A* **89**, 012117 (2014).

[66] S. J. van Enk and C. W. J. Beenakker, Measuring $\text{Tr}\rho^n$ on single copies of ρ using random measurements, *Phys. Rev. Lett.* **108**, 110503 (2012).

[67] D. M. Greenberger, M. A. Horne, and A. Zeilinger, Going beyond Bell's theorem, in **Bell's Theorem, Quantum Theory and Conceptions of the Universe** (Kluwer Academic Publishers, Amsterdam, NL, 1989) pp. 69–72.

[68] J.-P. Escofier, **Galois Theory** (Springer-Verlag, New York, NY, 2001).

[69] Link for the Newton's identity algorithm that recovers the spectrum from the polynomials:, <https://github.com/Rumoa/example-f1> (2022).

[70] W. Bruzda, V. Cappellini, H.-J. Sommers, and K. Życzkowski, Random quantum operations, *Phys. Lett. A* **373**, 320 (2009).

[71] M. Keyl and R. F. Werner, Estimating the spectrum of a density operator, *Phys. Rev. A* **64**, 052311 (2001).

[72] R. Alicki, S. Rudnicki, and S. Sadowski, Symmetry properties of product states for the system of N n -level atoms, *J. Math. Phys.* **29**, 1158 (1988).

[73] J. Wright, **How to learn a quantum state**, Ph.D. thesis, Carnegie Mellon University (2016).

[74] R. O'Donnell and J. Wright, Quantum spectrum testing, in **Proceedings of the forty-seventh annual ACM symposium on Theory of computing** (ACM, 2015) pp. 529–538.

[75] R. O'Donnell and J. Wright, Efficient quantum tomography, in **Proceedings of the forty-eighth annual ACM symposium on Theory of Computing** (ACM, 2016) pp. 899–912.

[76] J. Haah, A. W. Harrow, Z. Ji, X. Wu, and N. Yu, Sample-optimal tomography of quantum states, in **Proceedings of the forty-eighth annual ACM symposium on Theory of Computing** (ACM, 2016) pp. 913–925.

[77] H. Yuen, An improved sample complexity lower bound for (fidelity) quantum state tomography, *Quantum* **7**, 890 (2023).

[78] D. Bacon, I. L. Chuang, and A. W. Harrow, Efficient quantum circuits for Schur and Clebsch-Gordan transforms, *Phys. Rev. Lett.* **97**, 170502 (2006).

[79] M. E. Beverland, J. Haah, G. Alagic, G. K. Campbell, A. M. Rey, and A. V. Gorshkov, Spectrum estimation of density operators with Alkaline-Earth atoms, *Phys. Rev. Lett.* **120**, 025301 (2018).

[80] E. F. Galvão and D. J. Brod, Quantum and classical bounds for two-state overlaps, *Phys. Rev. A* **101**, 062110 (2020).

[81] R. Wagner, R. S. Barbosa, and E. F. Galvão, Inequalities witnessing coherence, nonlocality, and contextuality, arXiv:2209.02670 [quant-ph] (2022).

[82] D. R. M. Arvidsson-Shukur, J. C. Drori, and N. Y. Halpern, Conditions tighter than noncommutation needed for nonclassicality, *J. Phys. A* **54**, 284001 (2021).

[83] S. De Bièvre, Complete incompatibility, support uncertainty, and Kirkwood-Dirac nonclassicality, *Phys. Rev. Lett.* **127**, 190404 (2021).

[84] J. Xu, Classification of incompatibility for two orthonormal bases, *Phys. Rev. A* **106**, 022217 (2022).

[85] J. Xu, Kirkwood-Dirac classical pure states, arXiv:2210.02876 [quant-ph] (2022).

[86] R. Wagner, A. Camillini, and E. F. Galvão, Coherence and contextuality in a Mach-Zehnder interferometer, arXiv:2210.05624 [quant-ph] (2022).

[87] A. E. Jones, S. Kumar, S. D'Aurelio, M. Bayerbach, A. J. Menssen, and S. Barz, Distinguishability and mixedness in quantum interference, arXiv:2201.04655 [quant-ph] (2022).

[88] T. Bitter and D. Dubbers, Manifestation of Berry's topological phase in neutron spin rotation, *Phys. Rev. Lett.* **59**, 251 (1987).

[89] D. Suter, K. T. Mueller, and A. Pines, Study of the Aharonov-Anandan quantum phase by NMR interferometry, *Phys. Rev. Lett.* **60**, 1218 (1988).

[90] J. Harris, B. Yan, and N. A. Sinitsyn, Benchmarking information scrambling, *Phys. Rev. Lett.* **129**, 050602 (2022).

Appendix A: Formal comparison between standard weak measurement and circuit protocol

In this section, we estimate the sample complexity of finding weak values using the Bargmann invariants scheme and compare it with the sample complexity of measuring weak values using the standard protocol, known as weak measurement. Operationally, the two procedures are drastically different, which makes the comparison in terms of purely complexity arguments difficult. Therefore, for simplicity of the argument, we consider observables $A = |a\rangle\langle a|$. Recall that weak values can be written as

$$A_w = \frac{\Delta_3(\phi, a, \psi)}{\Delta_2(\phi, \psi)}. \quad (\text{A1})$$

1. Same number of samples for numerator and denominator

In order to compute A_w with the cycle test, we must compute the quantities in the numerator and denominator separately: using the SWAP-test for one and the cycle test associated with the operator C_3 for the other. We can focus solely on the complexity of estimating the real part A_w . The same analysis can be repeated for the imaginary part. Then, since $\Delta_2(\phi, \psi)$ is real, we must determine the sample complexity related to estimating the quantity $\text{Re}[A_w] = \text{Re}[\Delta_3(\phi, a, \psi)]/\Delta_2(\phi, \psi)$, i.e., we can focus on the real part of $\Delta_3(\phi, a, \psi)$ for the estimation of the numerator of A_w .

The results provided by runs of such tests can be described by random variables X_i taking values in $\{\pm 1\}$, with i denoting each run. Denoting by $p_+ = (1 + \text{Re}[\Delta_3(\phi, a, \psi)])/2$ and $p_- = 1 - p_+$ the probabilities of X_i being $+1$ and -1 , respectively, we write X_i 's expectation value as $\mathbb{E}[X_i] = +p_+ - p_- = \text{Re}[\Delta_3(\phi, a, \psi)]$.

Assuming we have $N^{(3)}$ runs associated with X_i , where superscript (3) refers to the fact that we are estimating third-order invariant, we consider the total random variable $X := \sum_{i=1}^{N^{(3)}} X_i$. By linearity of \mathbb{E} , $\mathbb{E}[X] = N^{(3)}\text{Re}[\Delta_3(\phi, a, \psi)]$. We, then, apply Hoeffding's inequality, a standard method in learning theory and statistical analysis [47, 48]. According to this bound, if a_i and b_i are real constants such that $a_i \leq X_i \leq b_i$ for every $i \in \{1, \dots, N\}$ and $X = \sum_i X_i$, we have that, for any $t > 0$,

$$\mathbb{P}[|X - \mathbb{E}[X]| \geq t] \leq 2 \exp\left(-\frac{2t^2}{\sum_{i=1}^{N^{(3)}} (b_i - a_i)^2}\right). \quad (\text{A2})$$

In our case, $a_i = -1$ and $b_i = +1$ for every i , which allows us to rewrite the above expression as

$$\mathbb{P}\left[|X - N^{(3)}\text{Re}[\Delta_3(\phi, a, \psi)]| \geq t\right] \leq 2e^{-2t^2/4N^{(3)}}, \quad (\text{A3})$$

which implies that

$$\mathbb{P}\left[\left|\frac{X}{N^{(3)}} - \text{Re}[\Delta_3(\phi, a, \psi)]\right| \geq \frac{t}{N^{(3)}}\right] \leq 2e^{-t^2/2N^{(3)}}. \quad (\text{A4})$$

Defining $\delta^{(3)} := 2e^{-t^2/2N^{(3)}}$, we get that $\delta^{(3)}/2 = e^{-t^2/2N^{(3)}} \Rightarrow t = \sqrt{2N^{(3)} \ln(2/\delta^{(3)})}$. Hence, we can ensure that, with probability greater than $1 - \delta^{(3)}$, the estimator $X/N^{(3)}$ gives the true value of the real third-order invariant within an error of $\sqrt{2 \ln(2/\delta^{(3)})/N^{(3)}}$, i.e.,

$$\mathbb{P}\left[\left|\frac{X}{N^{(3)}} - \text{Re}[\Delta_3(\phi, a, \psi)]\right| \geq \sqrt{\frac{2 \ln(2/\delta^{(3)})}{N^{(3)}}}\right] \leq \delta^{(3)}. \quad (\text{A5})$$

Similarly, we can introduce random variables Y_i for $N^{(2)}$ runs of the SWAP test, each with expectation $\mathbb{E}[Y_i] = \Delta_2(\phi, \psi)$, and the respective counterpart of other

relevant parameters to write

$$\mathbb{P}\left[\left|\frac{Y}{N^{(2)}} - \Delta_2(\phi, \psi)\right| \geq \sqrt{\frac{2 \ln(2/\delta^{(2)})}{N^{(2)}}}\right] \leq \delta^{(2)}, \quad (\text{A6})$$

where we have used the fact that $\Delta_2(a, b) \equiv \text{Re}[\Delta_2(a, b)]$ for any pair of states $|a\rangle, |b\rangle \in \mathcal{H}$.

In our protocol, we have two different procedures: one in which we use $N^{(3)}$ samples to estimate $\text{Re}[\Delta_3(\phi, a, \psi)]$ and another in which we use $N^{(2)}$ samples to estimate $\Delta_2(\phi, \psi)$. Defining $\varepsilon^{(n)} := \sqrt{2 \ln(2/\delta^{(2)})/N^{(2)}}$, we can write

$$\Delta_2(\phi, \psi) - \varepsilon^{(2)} \leq \frac{Y}{N^{(2)}} \leq \Delta_2(\phi, \psi) + \varepsilon^{(2)} \quad (\text{A7})$$

or simply

$$\left|\frac{Y}{N^{(2)}}\right| \geq |\Delta_2(\phi, \psi) - \varepsilon^{(2)}|. \quad (\text{A8})$$

At first, let us assume that we have equal choices for the precision with a high probability of learning the related second- and third-order invariants, i.e., $\varepsilon^{(2)} = \varepsilon^{(3)} \equiv \varepsilon$ and $\delta^{(2)} = \delta^{(3)} \equiv \delta$. This implies that $N^{(2)} = N^{(3)} \equiv N$. Then, with a probability greater than $1 - 2\delta$, we have

$$\begin{aligned} \left|\frac{X}{Y} - \frac{\text{Re}[\Delta_3(\phi, a, \psi)]}{\Delta_2(\phi, \psi)}\right| &= \\ &= \left|\frac{\frac{X}{N} \Delta_2 - \frac{Y}{N} \text{Re}[\Delta_3]}{\frac{Y}{N} \Delta_2}\right| \\ &= \left|\frac{\frac{X}{N} \Delta_2 - \Delta_2 \text{Re}[\Delta_3] + \Delta_2 \text{Re}[\Delta_3] - \frac{Y}{N} \text{Re}[\Delta_3]}{\frac{Y}{N} \Delta_2}\right| \\ &\leq \frac{\Delta_2 \left|\frac{X}{N} - \text{Re}[\Delta_3]\right| + |\text{Re}[\Delta_3]| \left|\frac{Y}{N} - \Delta_2\right|}{\Delta_2 \frac{Y}{N}} \\ &\leq \frac{\Delta_2 \varepsilon + |\text{Re}[\Delta_3]| \varepsilon}{\Delta_2 |\Delta_2 - \varepsilon|} = \frac{1 + |\text{Re}[A_w]|}{\left|\frac{\Delta_2}{\varepsilon} - 1\right|}. \end{aligned} \quad (\text{A9})$$

In the last inequality, we have used that $|Y/N| \geq |\Delta_2 - \varepsilon|$, as seen in Eq. (A8). In the above expression, we have also simplified the notation using $\Delta_2 \equiv \Delta_2(\phi, \psi)$ and $\Delta_3 \equiv \Delta_3(\phi, a, \psi)$. As a result, we conclude that

$$\mathbb{P}\left[\left|\frac{X}{Y} - \text{Re}[A_w]\right| \geq \frac{1 + |\text{Re}[A_w]|}{\left|\frac{\Delta_2}{\varepsilon} - 1\right|}\right] \leq 2\delta, \quad (\text{A10})$$

i.e., the resulting accuracy ε_T of estimating the real part of the weak value is

$$\varepsilon_T = \frac{1 + |\text{Re}[A_w]|}{\left|\frac{\Delta_2}{\varepsilon} - 1\right|}. \quad (\text{A11})$$

Since $\varepsilon = \sqrt{\ln(2/\delta)/N}$, we see that the number of samples needed scales as

$$N = O\left(\frac{\ln(2/\delta) |\text{Re}[A_w]|^2}{\Delta_2^2 \varepsilon_T^2}\right). \quad (\text{A12})$$

This allows us to compare the sample complexity of measuring weak values using the cycle test with the sample complexity associated with weak measurement schemes. In the standard weak measurement, one has a successful post-selection given by $N_s = |\langle \phi | \psi \rangle|^2 N$ with N the total number of samples used. For the successful incidents, the measurement outcomes are assumed to be Gaussian distributed with variance satisfying $\sigma_i^2 \gg \gamma^2 |A_w|^2$. Then, for every $i \in \{1, \dots, N_s\}$, $\mathbb{E}[X_i] = \gamma \text{Re}[A_w]$. For simplicity, let us choose $\sigma_i^2 = C\gamma^2 |A_w|^2$ for every i , where C is a large constant factor. We have therefore the random variable $X = \sum_{i=1}^{N_s} X_i$ for the successful attempts, for which it holds that $\mathbb{E}[X] = N_s \gamma \text{Re}[A_w]$ and $\text{Var}[X] = N_s \sigma_i^2 = CN_s \gamma^2 |A_w|^2$, assuming that all successful events are independent. Given that $\mathbb{E}[X/N_s \gamma] = \text{Re}[A_w]$ and because the distribution of successful incidents is Gaussian distributed, we have that the probability within a certain region is guaranteed by the error function

$$\mathbb{P} \left[\left| \frac{X}{\gamma N_s} - \text{Re}[A_w] \right| \geq \varepsilon \right] \leq 1 - \text{erf} \left(\frac{\varepsilon}{\sqrt{2\text{Var}(X/\gamma N_s)}} \right). \quad (\text{A13})$$

To simplify the notation, we use that $\text{Var}(X/\gamma N_s) = \text{Var}(X)/\gamma^2 N_s^2 = C|A_w|^2/N_s$ and define

$$\delta := \text{erfc} \left(\sqrt{\frac{\varepsilon^2 \Delta_2 N}{2C|A_w|^2}} \right), \quad (\text{A14})$$

where $\text{erfc}(x) = 1 - \text{erf}(x)$ is the complement of the error function. Then, the necessary total number of samples

N to estimate $\text{Re}[A_w]$ using $X/\gamma N_s$ is

$$N = 2C(\text{erfc}^{-1}(\delta))^2 \frac{|A_w|^2}{\varepsilon^2 \Delta_2}, \quad (\text{A15})$$

which gives an order of samples better than the case of the cycle test when $\Delta_2 \rightarrow 0$ since, in this case,

$$N^{(\text{weak})} = O \left(\text{erfc}^{-1}(\delta)^2 \frac{|A_w|^2}{\varepsilon^2 \Delta_2} \right). \quad (\text{A16})$$

This implies that there might be no complex theoretic advantage in using the cycle test protocol to implement weak value amplification, for which $\Delta_2(\phi, \psi)$ must be extremely small. However, this does not exclude the possibility that, for specific setups, there might be benefits in using the cycle test—e.g., in cases where the constant C related to the weak coupling is exponentially big. As pointed out in the main text, for simply witnessing *nonclassical values*, the cycle test *does* provide a sample complexity advantage since one does not need to estimate $\Delta_2(\phi, \psi)$. In particular, this feature might be interesting in specific setups of quantum sensing using the imaginary part of weak values.

2. Different number of samples for numerator and denominator

Given that we expect $\Delta_2(\phi, \psi) \ll 1$ in various applications of weak values, e.g., weak value amplification, it is relevant to consider the use of more samples to estimate the overlap such that $N^{(2)} > N^{(3)}$. We can, therefore, analyze this particular situation to observe if (and how) the sample complexity of estimating the weak value changes.

If we do not assume that $N^{(2)} = N^{(3)}$, we have

$$\begin{aligned} \left| \frac{X}{Y} - \frac{N^{(3)} \text{Re}[\Delta_3(\phi, a, \psi)]}{N^{(2)} \Delta_2(\phi, \psi)} \right| &= \left| \frac{N^{(2)} \Delta_2(\phi, \psi) X - N^{(3)} \text{Re}[\Delta_3(\phi, a, \psi)] Y}{Y N^{(2)} \Delta_2(\phi, \psi)} \right| = \\ &= \left| \frac{N^{(2)} \Delta_2(\phi, \psi) X - N^{(2)} N^{(3)} \Delta_2(\phi, \psi) \text{Re}[\Delta_3(\phi, a, \psi)] + N^{(2)} N^{(3)} \Delta_2(\phi, \psi) \text{Re}[\Delta_3(\phi, a, \psi)] - N^{(3)} \text{Re}[\Delta_3(\phi, a, \psi)] Y}{Y N^{(2)} \Delta_2(\phi, \psi)} \right| \\ &\leq \frac{|N^{(2)} \Delta_2(\phi, \psi) X - N^{(2)} N^{(3)} \Delta_2(\phi, \psi) \text{Re}[\Delta_3(\phi, a, \psi)]| + |N^{(2)} N^{(3)} \Delta_2(\phi, \psi) \text{Re}[\Delta_3(\phi, a, \psi)] - N^{(3)} \text{Re}[\Delta_3(\phi, a, \psi)] Y|}{Y N^{(2)} \Delta_2(\phi, \psi)} \\ &= \frac{N^{(2)} \Delta_2(\phi, \psi) |X - N^{(3)} \text{Re}[\Delta_3(\phi, a, \psi)]| + N^{(3)} |\text{Re}[\Delta_3(\phi, a, \psi)]| |N^{(2)} \Delta_2(\phi, \psi) - Y|}{Y N^{(2)} \Delta_2(\phi, \psi)}. \end{aligned} \quad (\text{A17})$$

Hoeffding's inequality leads to

$$\mathbb{P}[|X - N^{(3)} \text{Re}[\Delta_3(\phi, a, \psi)]| \geq \sqrt{2N^{(3)} \ln(2/\delta^{(3)})}] \leq \delta^{(3)} \quad (\text{A18})$$

and

$$\mathbb{P}[|Y - N^{(2)} \Delta_2(\phi, \psi)| \geq \sqrt{2N^{(2)} \ln(2/\delta^{(2)})}] \leq \delta^{(2)}, \quad (\text{A19})$$

implying that, with probability $\geq 1 - \delta^{(2)}$,

$$\frac{1}{Y} \leq \frac{1}{N^{(2)} \Delta_2(\phi, \psi) - \sqrt{2N^{(2)} \ln(2/\delta^{(2)})}} \approx \frac{1}{N^{(2)} \Delta_2(\phi, \psi)} \quad (\text{A20})$$

for a sufficiently large $N^{(2)}$. In turn, this leads to

$$\begin{aligned} \left| \frac{X}{Y} - \frac{N^{(3)} \operatorname{Re}[\Delta_3(\phi, a, \psi)]}{N^{(2)} \Delta_2(\phi, \psi)} \right| &\leq \frac{N^{(2)} \Delta_2(\phi, \psi) \sqrt{2N^{(3)} \ln(2/\delta^{(3)})} + N^{(3)} |\operatorname{Re}[\Delta_3(\phi, a, \psi)]| \sqrt{2N^{(2)} \ln(2/\delta^{(2)})}}{N^{(2)} N^{(3)} \Delta_2(\phi, \psi)^2} \\ \left| \frac{X}{Y} - \frac{N^{(3)} \operatorname{Re}[\Delta_3(\phi, a, \psi)]}{N^{(2)} \Delta_2(\phi, \psi)} \right| &\leq \frac{\sqrt{N^{(3)}}}{N^{(2)} \Delta_2(\phi, \psi)} \sqrt{2 \ln(2/\delta^{(3)})} + \frac{N^{(3)}}{(N^{(2)})^{3/2} \Delta_2(\phi, \psi)^2} |\operatorname{Re}[\Delta_3(\phi, a, \psi)]| \sqrt{2 \ln(2/\delta^{(2)})}, \end{aligned} \quad (\text{A21})$$

from which we conclude that

$$\left| \frac{\frac{X}{N^{(3)}}}{\frac{Y}{N^{(2)}}} - \frac{\operatorname{Re}[\Delta_3(\phi, a, \psi)]}{\Delta_2(\phi, \psi)} \right| = \frac{N^{(2)}}{N^{(3)}} \left| \frac{X}{Y} - \frac{N^{(3)} \operatorname{Re}[\Delta_3(\phi, a, \psi)]}{N^{(2)} \Delta_2(\phi, \psi)} \right| \leq \underbrace{\frac{\sqrt{2 \ln(2/\delta^{(3)})}}{\sqrt{N^{(3)}} \Delta_2(\phi, \psi)} + \frac{|\operatorname{Re}[\Delta_3(\phi, a, \psi)]| \sqrt{2 \ln(2/\delta^{(2)})}}{\sqrt{N^{(2)}} \Delta_2(\phi, \psi)^2}}_{=:\varepsilon}. \quad (\text{A22})$$

Defining $\delta := \delta^{(2)} + \delta^{(3)}$, we write

$$\mathbb{P} \left[\left| \frac{\frac{X}{N^{(3)}}}{\frac{Y}{N^{(2)}}} - \frac{\operatorname{Re}[\Delta_3(\phi, a, \psi)]}{\Delta_2(\phi, \psi)} \right| \geq \varepsilon \right] \leq \delta. \quad (\text{A23})$$

Since we have already analyzed the case in which $N^{(2)} = N^{(3)}$, we now focus on the case in which they differ. Let us capture this difference with a parameter c , letting $N^{(2)} \sim N^{(3)}/\Delta_2(\phi, \psi)^c$. Since our main interest lies in scenarios $\Delta_2(\phi, \psi)$ is assumed to be small, we want to study the situation $N^{(2)} \gg N^{(3)}$ to see if we have some improvement in the sample complexity. Then, we assume c is positive and $\Delta_2(\phi, \psi)^2 \ll 1$. As a result, the total number of samples satisfies $N := N^{(2)} + N^{(3)} \simeq N^{(3)}/\Delta_2(\phi, \psi)^c$. This implies that

$$\varepsilon = \frac{\sqrt{2 \ln(2/\delta^{(3)})}}{\sqrt{N^{(3)}} \Delta_2(\phi, \psi)} + \frac{|\operatorname{Re}[\Delta_3(\phi, a, \psi)]| \sqrt{2 \ln(2/\delta^{(2)})}}{\sqrt{N^{(2)}} \Delta_2(\phi, \psi)^2} = \frac{\sqrt{2 \ln(4/\delta)}}{\sqrt{N}} \left(\frac{1}{\Delta_2(\phi, \psi)^{1+c/2}} + \frac{|\operatorname{Re}[\Delta_3(\phi, a, \psi)]|}{\Delta_2(\phi, \psi)^2} \right), \quad (\text{A24})$$

from which we can extract the dependency in the number of samples with precision ε in learning the real part of the weak value:

$$N \simeq \frac{2 \ln(4/\delta)}{\varepsilon^2} \left(\frac{1}{\Delta_2(\phi, \psi)^{1+c/2}} + \frac{|\operatorname{Re}[\Delta_3(\phi, a, \psi)]|}{\Delta_2(\phi, \psi)^2} \right)^2. \quad (\text{A25})$$

Finally, let us study the number of samples by considering the possible values of the parameter c :

1. Case $c = 2$: We have $1 + c/2 = 2$. Then, we are left with an order of number of samples equal to the one when we had $N^{(2)} = N^{(3)}$ since $N = \frac{2(\ln(4/\delta))}{\varepsilon^2 \Delta_2(\phi, \psi)^4} (1 + |\operatorname{Re}[\Delta_3(\phi, a, \psi)]|)^2$. Note that, in the results presented in the previous subsection, the number of samples refers to the estimation of the real part of the weak value while, here, it refers to the estimation of the third-order invariant. This is the reason for the difference seen in the order of the overlap.
2. Case $0 < c < 2$: Assuming that $|\operatorname{Re}[\Delta_3(\phi, a, \psi)]| = O(1)$ and that it does not scale with $\Delta_2(\phi, \psi)$, it follows that $|\operatorname{Re}[\Delta_3(\phi, a, \psi)]|/\Delta_2(\phi, \psi) \gg 1/\Delta_2(\phi, \psi)^{1+c/2}$ for small $\Delta_2(\phi, \psi)$. After substituting these approximations into the equation for N , we are left with the same sample complexity as before.
3. Case $c > 2$: Direct calculation leads to $N \simeq$

$\frac{2(\ln(4/\delta))}{\varepsilon^2 \Delta_2(\phi, \psi)^{2+c}}$, which is worse in sample complexity than the previous results, and worsens the larger the value the parameter c takes.

In summary, these calculations show that the sample complexity does not improve statistically if one estimates the overlaps with a larger, or even much larger, number of samples than the number of samples necessary to estimate the third-order invariant in the measurement of weak values.

Appendix B: Sample and measurement complexity of estimating the spectrum using the cycle-test

1. Proof of Lemma 2

To estimate $\{\operatorname{Tr}(\rho^2), \dots, \operatorname{Tr}(\rho^d)\}$, we want to learn with high probability $1 - \delta$ the entire set of estimators

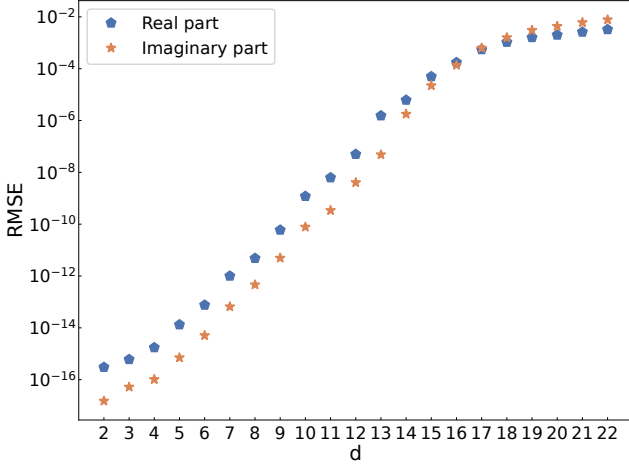


Figure 7. Aggregated root-mean-squared error (RMSE) spectrum estimation using the Faddeev-LeVerrier Algorithm. Eigenvalues of mixed states computed from multivariate traces $\{\text{Tr}(\rho^n)\}_{n=1}^d$ are compared with the ones obtained by diagonalization of the density matrix using *numpy*. For each dimension, a data set of random 1000 density matrices ρ is used. We sample the states using the Ginibre ensemble.

within an error ε . Using the union bound,

$$\begin{aligned} \mathbb{P} \left[\bigcup_{i=2}^d \left\{ \hat{\rho}^i : |\text{Tr}(\hat{\rho}^i) - \text{Tr}(\rho^i)| \geq \varepsilon \right\} \right] &\leq \\ &\leq \sum_{i=2}^d \mathbb{P} \left[|\text{Tr}(\hat{\rho}^i) - \text{Tr}(\rho^i)| \geq \varepsilon \right] \quad (B1) \\ &= (d-1) \mathbb{P} \left[|\text{Tr}(\hat{\rho}^i) - \text{Tr}(\rho^i)| \geq \varepsilon \right]. \end{aligned}$$

We fix $\mathbb{P} \left[|\text{Tr}(\hat{\rho}^i) - \text{Tr}(\rho^i)| \geq \varepsilon \right] = \delta/(d-1)$ such that the total error probability is δ .

From Hoeffding's inequality, for N independent samples $X_i \in [a, b]$ and mean estimator, the number of *statistical* samples needed to estimate each trace is, as already mentioned in Appendix A, $O(\ln(2/\delta)/\varepsilon^2)$. But each statistical sample requires $O(d^2)$ states to compute $\{\text{Tr}(\rho^2), \dots, \text{Tr}(\rho^d)\}$ using the cycle-test. The total number of states is, therefore, $Nd^2 = \frac{d^2}{\varepsilon^2} \ln \sqrt{2(d-1)/\delta}$ and, as a consequence, $N = O \left(\frac{d^2}{\varepsilon^2} \ln(d/\delta) \right)$ samples estimate the chosen set of traces to precision ε with probability $1 - \delta$. Since the number of measurements equals the number of statistical samples times d , which accounts for one measurement for each element in the set of traces, we have that the number of measurements is of order $O \left(\frac{d}{\varepsilon^2} \ln(d/\delta) \right)$. This concludes the proof.

In the main text, we reported the sample complexity $\tilde{O}(d^2/\varepsilon^2)$ that hides $\log(d)$ factors and fixed δ to be a reference value to prescribe what is meant by “high probability,” usually taken to be equal to $1 - \delta = 2/3$.

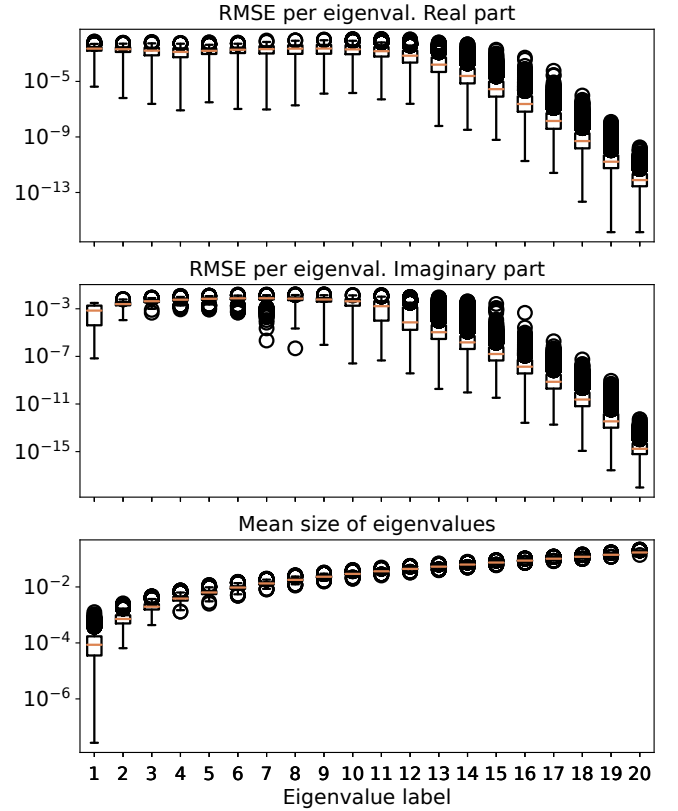


Figure 8. Mean size of eigenvalues and RMSE per eigenvalue. For 1000 random mixed density matrices of fixed Hilbert space dimension 20, we study the real and imaginary parts of the spectrum given from the Faddeev-LeVerrier algorithm.

2. Numerical analysis for the Faddeev–LeVerrier algorithm

In this section, we conduct a numerical study of the behavior of the Faddeev–LeVerrier algorithm [68, Chapter 3], which returns the estimates of the eigenvalues of ρ , given $\{\text{Tr}(\rho^i)\}_{i=2}^d$ as an input.

In Fig. 7, using noiseless experimental data, i.e. the traces $\{\text{Tr}(\rho^i)\}_i$, we show the aggregated RMSE of the real and imaginary parts of the spectrum of ρ . We compare the predicted spectrum with the one computed via diagonalization with *numpy*.

Ideally, the spectrum should be real-valued. However, as mentioned in the main text, numerical instabilities generate imaginary parts in the outputs of the algorithm. At a certain dimension, the RMSE of the imaginary part of all eigenvalues exceeds the one for the real part. This is expected, as numerical inaccuracies occur when very small roots need to be estimated. As a result, the aggregated RMSE for high dimensions can be orders of magnitude bigger than the actual size of some eigenvalues. In what follows, we study if the appearance of these imaginary values, as well as their size, significantly influences the comparison between the real part of the spectrum

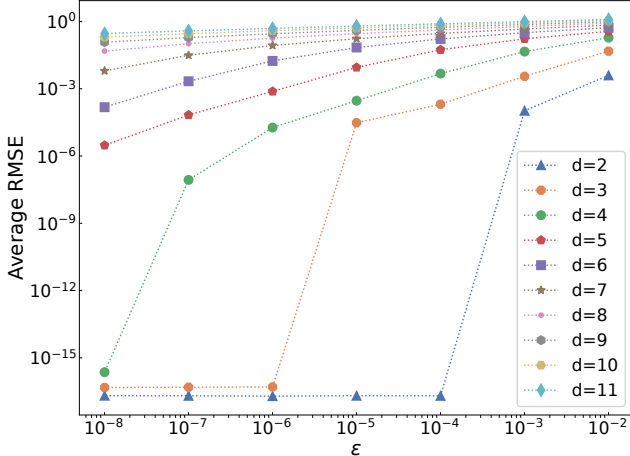


Figure 9. **Average RMSE of the imaginary parts of the spectrum estimation of 5000 random ρ .** This figure represents the imaginary counterpart of Fig. 4. Each matrix generates 1000 noisy samples to compute the RMSE.

and the ideal spectrum.

Let us take as a case study the error *per eigenvalue* for a sufficiently large Hilbert space dimension. In Fig. 8, we show the average size of the eigenvalues using 1000 random density matrices of dimension 20. The biggest eigenvalues have sizes of order 10^{-2} while the associated error between the real and imaginary part is smaller than 10^{-13} . On the other hand, the smallest eigenvalues have an error approximately equal to the size of the eigenvalue, which explains the aggregated RMSE from Fig. 7 in higher dimensions.

Although the predicted eigenvalues can contain non-negligible imaginary parts, their presence does not affect the prediction of the real parts. These imaginary values come from the presence of small coefficients in the characteristic polynomial. In Fig. 9, we show the RMSE of the imaginary part in the estimation of the spectrum using noisy data. The sudden increase for a certain dimension is closely related to the amount of noise introduced. For larger dimensions, smaller amounts of noise modify the coefficients enough to produce the appearance of imaginary values. However, by comparing with Fig. 4, the trend of the RMSE of real parts is not affected by these “bumps” in the imaginary parts, allowing us to safely discard them from the predictions.

a. Learning the largest eigenvalue

As smaller eigenvalues produce bigger errors, the Faddeev–LeVerrier algorithm can be used to estimate only the largest eigenvalues. In Fig. 10, we show the RMSE of the real part in the prediction of the largest eigenvalue using the same noisy dataset as the one used for the prediction of the entire spectrum. Since the

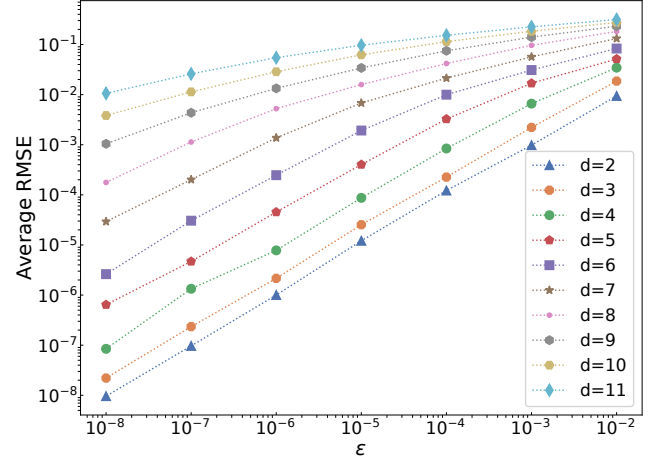


Figure 10. **Average RMSE of the real part of largest eigenvalue for 5000 random density matrices.** Each matrix generates 1000 noisy samples to compute the RMSE. We see that, when focusing on the largest eigenvalue, the accuracy of the estimation improves when compared to the results for the entire spectrum estimation from Fig. 4 in the main text.

largest eigenvalue depends mostly on the coefficients of the highest order, the size of these makes them less sensitive to the noise and allows the obtaining of a RMSE of 10^{-3} in dimension 6 with an error $\varepsilon = 10^{-4}$ for the traces. However, as stated in the main text, computing the entire set of traces is not recommended in this task as higher powers in the traces of ρ are more difficult to estimate and contribute less to the largest eigenvalue.

Appendix C: Proof of Lemma 6

Consider a general triplet of pure states $\{|\psi_1\rangle, |\psi_2\rangle, |\psi_3\rangle\}$ real with respect to some basis and choose the following parametrization for it:

$$\begin{aligned} |\psi_1\rangle &= |0\rangle \\ |\psi_2\rangle &= \cos(\beta)|0\rangle + \sin(\beta)|1\rangle \\ |\psi_3\rangle &= \cos(\gamma)|0\rangle + \sin(\gamma)\sin(\alpha)|1\rangle + \sin(\gamma)\cos(\alpha)|2\rangle, \end{aligned} \quad (C1)$$

where $\beta, \gamma \in [0, \pi]$ and $\alpha \in [0, 2\pi)$. Under this choice, made without loss of generality, we can define the function

$$\begin{aligned} h_1(\alpha, \beta, \gamma) &= -\Delta_2(\psi_1, \psi_2) + \Delta_2(\psi_1, \psi_3) + \Delta_2(\psi_2, \psi_3), \\ h_2(\alpha, \beta, \gamma) &= +\Delta_2(\psi_1, \psi_2) - \Delta_2(\psi_1, \psi_3) + \Delta_2(\psi_2, \psi_3), \\ h_3(\alpha, \beta, \gamma) &= +\Delta_2(\psi_1, \psi_2) + \Delta_2(\psi_1, \psi_3) - \Delta_2(\psi_2, \psi_3), \end{aligned} \quad (C2)$$

where each overlap depends on the variables α, β, γ . We can, then, study what the constraints $h_i > 1$ represent,

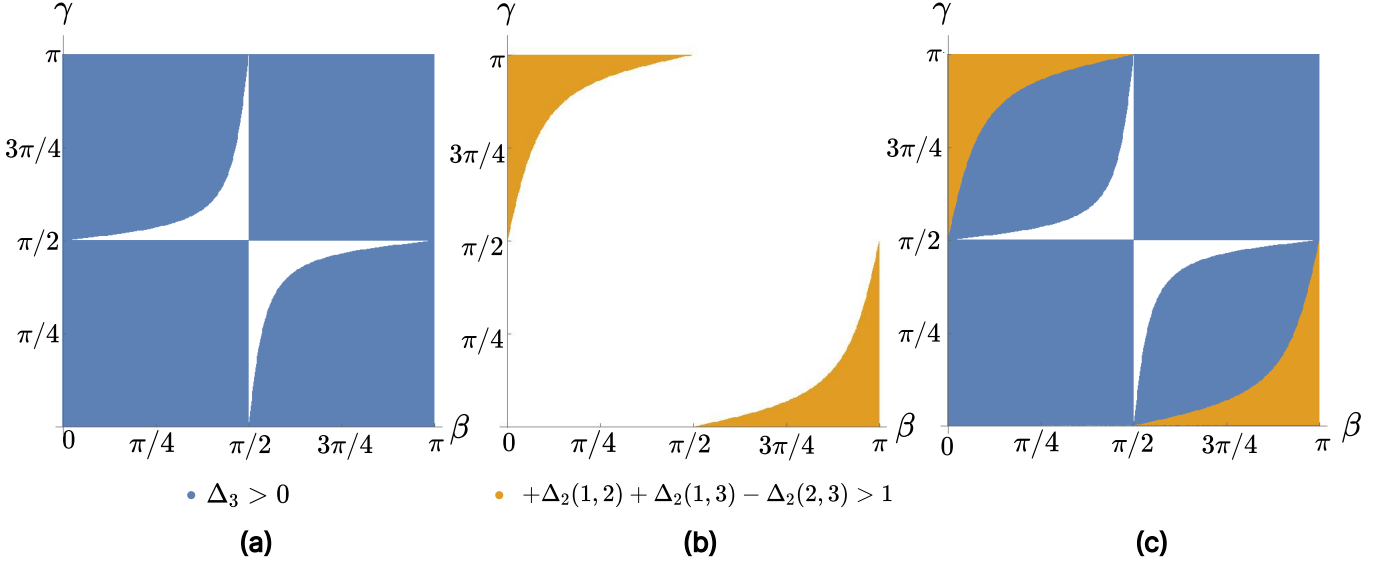


Figure 11. **Witnesses of third-order positivity.** (a) The white regions in the center are the area corresponding to $\Delta_3 \leq 0$. The blue region is given by $\Delta_3(\alpha, \beta, \gamma) > 0$ for $\alpha = 0.11$. (b) The light-brown region overlaps with the blue region completely, and it is given by $h_3(\alpha, \beta, \gamma) - 1 > 0$, showing that this condition implies $\Delta_3(\alpha, \beta, \gamma) > 0$. However, the converse does not necessarily hold. In fact, it is true only for $\alpha \in [0, \pi]$, as can be seen in (c), where we combine both configurations (a) and (b).

i.e.,

$$\begin{aligned}
 h_1 > 1 \Rightarrow \\
 0 < & -1 - \cos^2(\beta) + \cos^2(\gamma) + \cos^2(\beta) \cos^2(\gamma) + \\
 & + \sin^2(\beta) \sin^2(\gamma) \underbrace{\sin^2(\alpha)}_{\in [0, 1]} + \frac{1}{2} \sin(2\beta) \sin(2\gamma) \sin(\alpha) \\
 \leq & -1 - \cos^2(\beta) + \cos^2(\gamma) + \cos^2(\beta) \cos^2(\gamma) + \\
 & + \sin^2(\beta) \sin^2(\gamma) + \frac{1}{2} \sin(2\beta) \sin(2\gamma) \sin(\alpha) \\
 = & -2 \cos^2(\beta) + 2 \cos^2(\beta) \sin^2(\gamma) \\
 & + \frac{1}{2} \sin(2\beta) \sin(2\gamma) \sin(\alpha) \\
 = & -2 \cos^2(\beta) + 2 \Delta_3(\alpha, \beta, \gamma) \leq 2 \Delta_3(\alpha, \beta, \gamma), \tag{C3}
 \end{aligned}$$

which implies that $\Delta_3(\alpha, \beta, \gamma) \equiv \Delta_3(\psi_1, \psi_2, \psi_3) > 0$, where we have used that

$$\begin{aligned}
 \Delta_3(\alpha, \beta, \gamma) &= \langle \psi_1 | \psi_2 \rangle \langle \psi_2 | \psi_3 \rangle \langle \psi_3 | \psi_1 \rangle \\
 &= \cos^2(\beta) \cos^2(\gamma) + \frac{1}{4} \sin(2\beta) \sin(2\gamma) \sin(\alpha). \tag{C4}
 \end{aligned}$$

The same reasoning applies for $h_2 > 1$. For $h_3 > 1$, the situation is less straightforward since the two functions $h_3(\alpha, \beta, \gamma) - 1$ and $\Delta_3(\alpha, \beta, \gamma)$ are not totally ordered in the domain $[0, 2\pi] \times [0, \pi]^2$. However, we can analyze what $\Delta_3(\alpha, \beta, \gamma) > 0$ corresponds to in terms of the parameters β and γ when α lies in some domains. From the above, it follows that

$$\tan(\beta) \tan(\gamma) > -\frac{1}{\sin(\alpha)} \Rightarrow \Delta_3(\alpha, \beta, \gamma) > 0 \tag{C5}$$

if $\alpha \in [0, \pi]$. The case in which $\alpha \in [\pi, 2\pi]$ can be treated similarly. The function $h_3(\alpha, \beta, \gamma) - 1$ can be written as

$$\begin{aligned}
 h_3(\alpha, \beta, \gamma) - 1 &= \\
 &= -1 + \cos^2(\beta) + \cos^2(\gamma) - \cos^2(\beta) \cos^2(\gamma) \\
 &- \sin^2(\beta) \sin^2(\gamma) \sin^2(\alpha) - \frac{1}{2} \sin(2\beta) \sin(2\gamma) \sin(\alpha) \\
 &= -\sin^2(\beta) \sin^2(\gamma) - \sin^2(\beta) \sin^2(\gamma) \sin^2(\alpha) \\
 &\quad - \frac{1}{2} \sin(2\beta) \sin(2\gamma) \sin(\alpha) \\
 &= -\sin^2(\beta) \sin^2(\gamma) (1 + \sin^2(\alpha)) \\
 &\quad - \frac{1}{2} \sin(2\beta) \sin(2\gamma) \sin(\alpha). \tag{C6}
 \end{aligned}$$

The condition that $h_3(\alpha, \beta, \gamma) - 1 > 0$ implies that $\sin^2(\beta) \sin^2(\gamma) (1 + \sin^2(\alpha)) < -\sin(2\beta) \sin(2\gamma) \sin(\alpha)/2$.

Lemma 7. For any $\alpha, \beta, \gamma \in [0, \pi]$, if

$$\sin^2(\beta) \sin^2(\gamma) (1 + \sin^2(\alpha)) < -\frac{1}{2} \sin(2\beta) \sin(2\gamma) \sin(\alpha), \tag{C7}$$

then

$$\tan(\beta) \tan(\gamma) > -\frac{1}{\sin(\alpha)}. \tag{C8}$$

Proof. This lemma can be easily seen to hold numerically. In the range of $\alpha, \beta, \gamma \in [0, \pi]$ we see that there is always an overlap between the region for which the first inequality is satisfied simultaneously with the second inequality. The converse is not necessarily true. \square

The above lemma together with Eq. (C5) implies that $h_3 - 1 > 0 \Rightarrow \Delta_3 > 0$, as we wanted to show. The case $\alpha \in [\pi, 2\pi]$ is treated similarly, as already mentioned.

Fixing $\alpha = 0.11$, Fig. 11 shows the region of values $(\beta, \gamma) \in [0, \pi]$ for which the third-order invariant

positivity can be witnessed from the overlap inequality. The region in the center corresponds to negative values of the third-order invariant and the two colored regions overlap for any value of α , meaning that the region $\Delta_2(\psi_1, \psi_2) + \Delta_2(\psi_1, \psi_3) - \Delta_2(\psi_2, \psi_3) > 1$ implies the other; while the contrary does not always hold.